

# Textural evolution of magma during the 9.4-ka trachytic explosive eruption at Kilian Volcano, Chaîne des Puys, France

M. Colombier<sup>1,2</sup> · L. Gurioli<sup>1</sup>  · T. H. Druitt<sup>1</sup> · T. Shea<sup>3</sup> · P. Boivin<sup>1,4</sup> · D. Miallier<sup>4</sup> · N. Cluzel<sup>1</sup>

Received: 30 March 2016 / Accepted: 4 January 2017 / Published online: 24 January 2017  
© Springer-Verlag Berlin Heidelberg 2017

**Abstract** Textural parameters such as density, porosity, pore connectivity, permeability, and vesicle size distributions of vesiculated and dense pyroclasts from the 9.4-ka eruption of Kilian Volcano, were quantified to constrain conduit and eruptive processes. The eruption generated a sequence of five vertical explosions of decreasing intensity, producing pyroclastic density currents and tephra fallout. The initial and final phases of the eruption correspond to the fragmentation of a degassed plug, as suggested by the increase of dense juvenile clasts (bimodal density distributions) as well as non-juvenile clasts, resulting from the reaming of a crater. In contrast, the intermediate eruptive phases were the results of more open-conduit conditions (unimodal density distributions, decreases in dense juvenile pyroclasts, and non-juvenile clasts). Vesicles within the pyroclasts are almost fully connected; however, there are a wide range of permeabilities, especially for the dense juvenile clasts. Textural analysis of the juvenile clasts reveals two vesiculation events: (1) an early nucleation event at low

decompression rates during slow magma ascent producing a population of large bubbles (>1 mm) and (2) a syn-explosive nucleation event, followed by growth and coalescence of small bubbles controlled by high decompression rates immediately prior to or during explosive fragmentation. The similarities in pyroclast textures between the Kilian explosions and those at Soufrière Hills Volcano on Montserrat, in 1997, imply that eruptive processes in the two systems were rather similar and probably common to vulcanian eruptions in general.

**Keywords** Vulcanian explosions · Dome · Density · Connectivity · Permeability · VSD

## Introduction

Silicic volcanic eruptions are driven by the decompression-induced exsolution of melt-dissolved volatiles. This causes magma vesiculation, expansion, and fragmentation, followed by high-velocity discharge of gas and entrained pyroclasts (e.g., Sparks 1978; Wilson et al. 1980; Jaupart and Allegre 1991; Jaupart 1996; Massol and Jaupart 1999; Slezin 2003; Gonnermann and Manga 2007). The eruptive behavior at a given volcano depends on physical parameters, such as magma decompression rate, vesiculation kinetics, degassing style (open versus closed), and fragmentation mechanism (e.g., Rust and Cashman 2011; Gonnermann and Houghton 2012; Degruyter et al. 2012; Nguyen et al. 2013 and references therein). These processes are recorded by physical properties of the deposits, such as grain size and componentry, and by the physical and textural parameters of the pyroclasts, such as density, total and connected porosities, permeability, crystallinity, vesicle and crystal size distributions, and vesicle and crystal number densities, as well as features such as vesicle shapes and orientations, and relationships between vesicles

Editorial responsibility: K.V. Cashman

✉ L. Gurioli  
l.gurioli@opgc.univ-bpclermont.fr

- <sup>1</sup> Université Clermont Auvergne -CNRS-IRD, OPGC, Laboratoire Magmas et Volcans, F-63100, Clermont-Ferrand, France
- <sup>2</sup> Department of Earth and Environmental Sciences, University of Munich, Theresienstr. 41/III, 80333 Munich, Germany
- <sup>3</sup> Department of Geology and Geophysics, SOEST, University of Hawaii, Honolulu, HI 96822, USA
- <sup>4</sup> Université Clermont Auvergne, Laboratoire de Physique Corpusculaire, CNRS/IN2P3, Campus Universitaire des Cèzeaux, TSA 60026, 63178 Aubière cedex, France

and crystals. The different parameters provide insights into the physical processes occurring during eruption (e.g., Gurioli et al. 2015 and references therein). Grain size analysis allows one to obtain the fragment population characteristics of the associated explosion, which can support a genetic interpretation of the pyroclastic deposits (fall versus flow) and a classification of the volcanic events, when combined with information about the dispersal and depositional features of the deposit (e.g., Fisher 1964; Walker 1971, 1973; Sheridan 1971; Sparks 1976; Fisher and Schmincke 1984; Cas and Wright 1987; Wohletz et al. 1989; Freundt and Rosi 1998; Fagents et al. 2013). Componentry analysis (the categorization of clasts as juvenile, non-juvenile, and composite fragments, White and Houghton 2006) provides information on the type of fragmentation (magmatic versus phreatomagmatic), the feeding system, and conduit processes (e.g., Wohletz 1983; Heiken and Wohletz 1985; Sheridan and Marshall 1983; Barberi et al. 1989; Taddeucci et al. 2002; Eychenne et al. 2015). The density distribution of pyroclasts of similar size reflects the integrated result of magma vesiculation taking place before, during, and after fragmentation (e.g., Houghton and Wilson 1989; Hoblitt and Harmon 1993; Polacci et al. 2003; Kueppers et al. 2005; Di Traglia et al. 2009; Shea et al. 2010a; Mueller et al. 2011; Barker et al. 2012; Bernard et al. 2015). Pyroclast porosity, vesicle size distribution, and vesicle number density provide constraints on the kinetics of melt degassing and outgassing and, by extension, on decompression history and eruption intensity (e.g., Mangan and Sisson 2000; Klug et al. 2002; Mourtada-Bonnefoi and Laporte 2004; Toramaru 2006; Gurioli et al. 2008; Cluzel et al. 2008; Carey et al. 2009; Shea et al. 2010b, 2011, 2012; Houghton et al. 2010; Giachetti et al. 2010; Rust and Cashman 2011; Alfano et al. 2012; Rotella et al. 2014). Vesicle connectivity and clast permeability, along with the relative degrees of vesicle coalescence and collapse, yield information on gas transport and escape from the magma, largely to fragmentation (e.g., Klug and Cashman 1996; Melnik and Sparks 2002; Rust and Cashman 2004, 2011; Wright et al. 2006, 2007, 2009; Platz et al. 2007; Takeuchi et al. 2008; Nakamura et al. 2008; Schipper et al. 2013; Polacci et al. 2014; Nguyen et al. 2014). Crystallinity and degree of crystal breakage also depend on magma ascent history (e.g., Hammer et al. 1999; Couch et al. 2003; Kennedy et al. 2005; Noguchi et al. 2006; Clarke et al. 2007; Giachetti et al. 2010; Martel 2012; Befus et al. 2014).

In this paper, we present a textural characterization of products from the Holocene explosive eruption of Kilian Volcano in the Chaîne des Puys of central France, in order to understand the processes taking place in the conduit during eruption and to reconstruct the dynamics of the eruption through time. The study was motivated particularly by the proximity of Kilian Volcano, and of the Chaîne des Puys in general, to the city of Clermont-Ferrand (140,000 inhabitants).

## Geological background

The Chaîne des Puys comprises about 80 Quaternary volcanoes and is one of the youngest products of intraplate alkaline volcanism in the French Massif Central (Boivin et al. 2009; Boivin and Thouret 2013; Martel et al. 2013). The chain is 30 km long north-south and 3–4 km wide. Edifices are mostly scoria cones, with a few maars, tuff rings, and trachytic lava domes (Fig. 1a).

Kilian Volcano is marked by an elongated 400 × 150-m-wide and 40-m-deep explosion crater located in the hills of the Puy des Grosmanaux (Glangeaud 1913; Fig. 1b). The walls of the crater are composed of trachyte and were enlarged by quarrying in Roman and Medieval times (Miallier et al. 2013a; Boivin et al. 2015). The crater is the source of a widespread trachytic pyroclastic apron (Fig. 2). Studies by Camus (1975) and Goër de Herve et al. (1994) divided the deposits into three phases: (1) a main explosive phase, (2) growth of a trachytic lava dome over the vent, and (3) explosive destruction of part of that dome.

The main explosive phase has been dated at  $9.40 \pm 0.20$  ka using  $^{14}\text{C}$  measurements on charred wood within the deposits (Miallier et al. 2012; BP data calibrated with IntCal09, Reimer et al. 2009). The deposits are distributed across the central part of the Chaîne des Puys (Baudry and Camus 1972; Camus 1975; Michon 1996; Boivin et al. 2009, Figs. 1a and 2). Detailed mapping is complicated by partial erosion, local forest cover, and multiple distribution lobes across complex topography (Fig. 2). Moreover, the Kilian deposits are easily confused with those from Vasset Volcano (Fig. 1a), which have a similar age, similar chemistry, and mineralogy and a partly overlapping distribution (Michon 1996; Boivin et al. 2009). The Kilian deposits are 5 m thick at the southern base of the Puy de Dôme, 1 km from the crater (Fig. 2). They mantle the Puy de Dôme edifice and are 1 m thick on the summit, 400 m above Kilian crater. They also mantle the Puy de Grosmanaux (Fig. 1b) to the east, Puy Besace (Fig. 1b) to the west, Puy Salomon and Puy Montchié (13.6 ka old, Fig. 1a, b, respectively) to the south (Miallier et al. 2013b), and Nid de la Poule (10 ka old, Fig. 1a) and the lava flows of Puy Pariou (10 ka old, Fig. 1a) to the north (Miallier et al. 2012). They are underlain by a paleosol pitted by bomb impact sags. Isolated blocks of trachyte, basalt, and granite on the surface of Puy Besace (Fig. 1b), 500 m west of Kilian crater, are interpreted as ballistics. The paleosol beneath the deposits contains pollen from the beginning of the Boreal period (Raynal et al. 1998). Possible Kilian tephtras have been identified on the Limagne plain east of the Chaîne des Puys (Vernet and Raynal 2008; Vernet 2013) and in Swiss lake sediments (Martini and Duret 1965) to the NE.

Camus (1975) and Camus et al. (1975) suggested that the main explosive phase of the eruption was caused by phreatomagmatic activity. Michon (1996) identified four

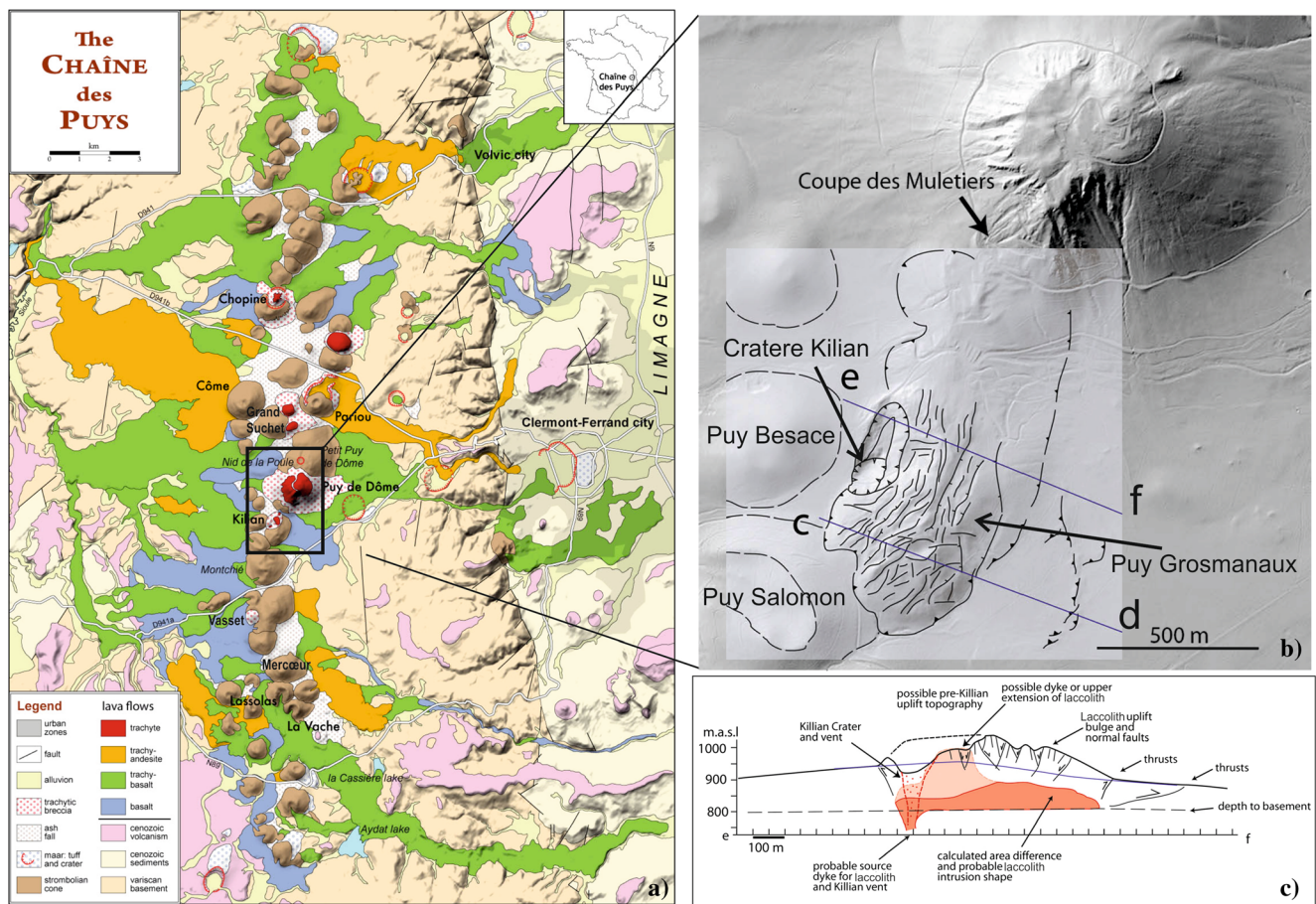


**Fig. 1** **a** Geological setting of the Chaîne des Puys (modified from Boivin et al. 2009). **b** Lidar-generated shaded relief image of the Kilian crater on the flank of the Puy Grosmanaux and the studied stratigraphic section (Coupe des Muletiers) on the southern flank of Puy de Dôme. The interpretative structural map, extracted from van Wyk de Vries et al. (2014), of the Kilian area is superimposed. **c** Cross section over profile e–f, with the Kilian Crater, to show how the intrusion managed to pierce

the surface on the NW side (probably above the feeder conduit) and subsequent vulcanian explosions from this conduit excavated the Kilian crater (modified from van Wyk de Vries et al. 2014). The profile c–d is not shown, but it is reported in Fig. 10c of van Wyk de Vries et al. (2014). The blue line is the hypothetical continuation of the thrusts indicated in the same figure

stratigraphic units (named DEF1K to DEF4K) and proposed the following sequence of events: (1) an initial phreatic vent-opening explosion, (2) explosion of an embryonic dome, (3) several phreatomagmatic vulcanian explosions, and (4) a large vulcanian explosion due to the decompression of a large dome.

The Puy des Grosmanaux was previously thought to be a simple cinder cone and associated lava flow (dated at about 46 ka by thermoluminescence; Guérin 1983). However, new Lidar data have shown that the edifice was uplifted to form a bulge cut by a major set of N-NE-trending faults and a lesser set of cross faults, the Kilian crater lying on the NW edge of the bulge (van Wyk de Vries et al. 2014 and Fig. 1c). The bulge has been attributed to a trachytic cryptodome that intruded and uplifted pre-existing strata, then partially vented through Kilian crater (van Wyk de Vries et al. 2014 and Fig. 1c). Indeed, a recent geophysical study (Portal et al. 2016) shows the presence of a dense, shallow trachytic body,

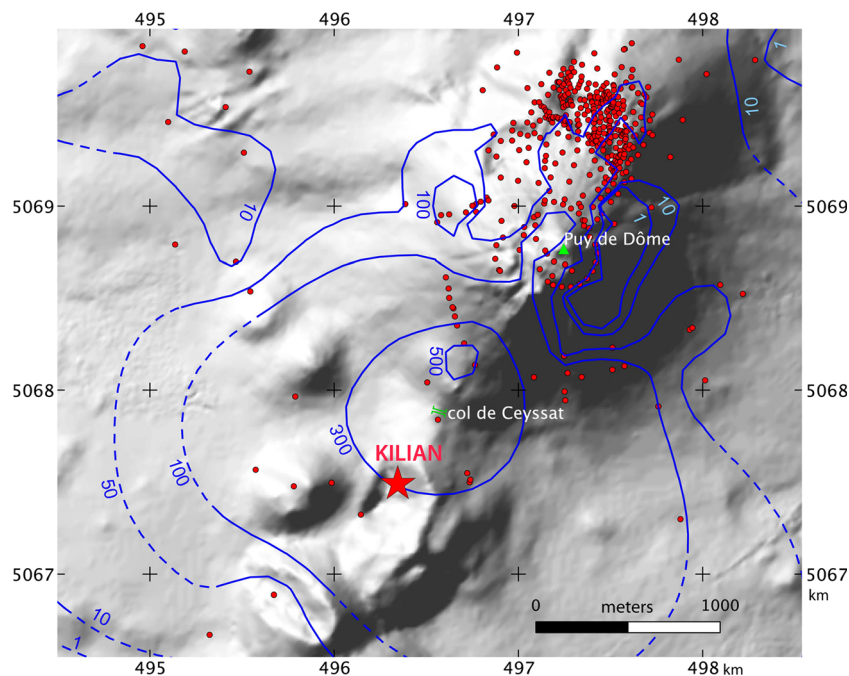
200 m width, below the crater of Kilian. The size of the dome matches the dimensions of the crater so the authors interpreted the dome as an intrusion filling the underlying conduit.

Magmas of the Chaîne des Puys range from alkali basalts to trachytes and are related by fractional crystallization (Maury et al. 1980; Villemant et al. 1981). A recent study based on phase equilibria, thermobarometry, and melt inclusion analysis determined the pre-eruptive storage conditions of the Kilian trachyte to be 300–400 MPa,  $775 \pm 20$  °C, and 7–8 wt% H<sub>2</sub>O (Martel et al. 2013).

### Methodology

We studied and sampled a 5-m-thick succession of proximal deposits from the eruption preserved in the “Coupe des Muletiers” outcrop about 1 km NNE of

**Fig. 2** Proximal dispersal of the Kilian deposits, with approximate total isopachs (in cm). The complications north of the Puy de Dôme are caused by the shadow effect of the latter edifice on pyroclastic density currents and by gravitational slides of units K1–K2 (see Fig. 3). *Red dots* = studied sections by previous field works. Coordinates are WGS84, UTM31N



Kilian crater (Figs. 1b and 3a) and now completely covered by a concrete wall.

The bulk major element composition of the juvenile clasts was measured by ICP-AES at the Laboratoire Magmas et Volcans (LMV) of Clermont-Ferrand. Glass compositions were measured on five clasts of varying density and crystal content, using a JXA-8500F hyperprobe at the University of Hawaii with a 10- $\mu\text{m}$  spot size, 15-kV accelerating voltage, and 10-nA beam current. The data are reported in Tables 1 and 2.

Bulk samples of the matrix of the eruption products were collected from a total of eight levels grouped into five stratigraphic units called U1, U2, U3, K1, and K2 from the base to the top (one to three levels per unit) and then were manually sieved at half phi intervals (Fig. 3b and Table 3). Particle componentry was carried out on the 4–8-mm-size fraction (around the main mode of the grain size analyses, Fig. 3b), because a sufficient fraction of clasts for this size was available for a statistically valid approach (Fig. 3c). For each level, we selected 60 to 163 juvenile particles within the 16–32-mm fraction for density and pycnometry measurements (Fig. 3d). This is the smallest granulometric fraction assumed to be representative of the larger size class in term of density (Houghton and Wilson 1989) and has been used in previous textural studies of fallout deposits, where the main grain size population is confined between 32 and 0.5 mm (e.g., Shea et al. 2010a). In addition, it is ideal for vesicle connectivity measurements (e.g., Formenti and Druitt 2003; Giachetti et al. 2010; Shea et al. 2012) and for avoiding possible effects of post-fragmentation expansion.

Textural measurements (density/porosity, connectivity, permeability, and acquisition of back-scattered electron detector

(BSE) images) were performed at the LMV. Densities of juvenile particles were measured by clast immersion in 200–400- $\mu\text{m}$ -diameter glass beads, based on a method described by Shimano and Nakada (2006), Nakamura et al. (2008), and Silva (2008). The glass bead technique provides a measure of the total volume of the particles. Dividing sample mass by volume yields a bulk density, which, when combined with the pore-free rock density, allows us to obtain the porosity  $\Phi$  of the sample (Table 4). The glass bead method was compared to the water immersion technique of Houghton and Wilson (1989), which is based on Archimedes' principle. We observed a good correlation between the two methods (Fig. 4), although densities obtained with glass beads are systematically higher than those obtained by water immersion. This is because the beads occupy the space of any large vesicles on the outside of the clast, which is not the case in the immersion method, where the clast is covered with a parafilm. Although the bead method is less time-consuming than water immersion, it yields higher clast density values if the fragments are characterized by external vesicles much larger than the beads. The average error for the Archimedes method is around 3% (see also Barker et al. 2012), while for the glass beads, it is less than 10% (Colombier 2013; Shimano and Nakada 2006).

A mean value for the vesicle-free rock density was determined by powdering clasts of varying bulk densities, measuring the volumes of known masses using an Accupyc 1340 Helium Pycnometer, then averaging. The same pycnometer was used to measure the connected porosity for each clast (Table 4) using the method of Formenti and Druitt (2003). We calculated the pore connectivity by dividing the connected porosity by the total porosity (Fig. 5a; Shimano and Nakada

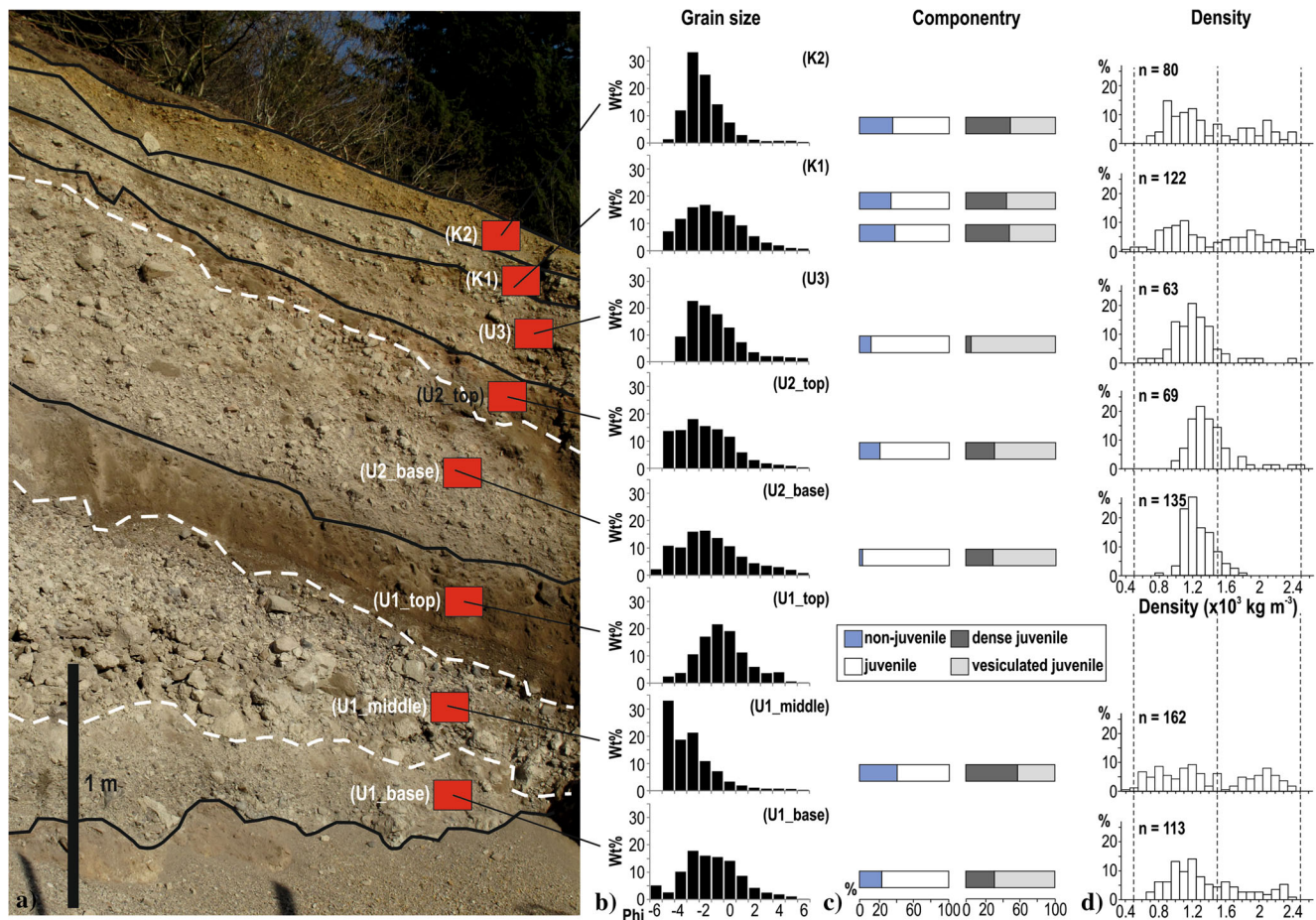


**Fig. 3** **a** The “Coupe des Muletiers” section. **b** Grain size histograms. **c** Componentry data. **d** Density distributions. *n* number of juvenile clasts measured for density in each layer

2006; Farquharson et al. 2015). A full description of the protocol for density and connectivity measurements is available at <http://www.obs.univ-bpclermont.fr/SO/televolc/dynvolc/index.php>.

Permeability measurements were performed on 18 pyroclasts selected from units U1, U3, K1, and K2. The largest clasts of known densities and vesicle connectivity values, covering a broad range of porosity (from 16 to 70%), were chosen (Fig. 5b). The clasts were cut into rectangular prisms to enable precise calculation of the cross-sectional area, which is required to calculate permeability. These prisms were then embedded in a viscous resin, which was left to harden for 24 h. The sample surface had been previously coated with a more viscous resin and then wrapped with parafilm to avoid intrusion of the less viscous resin inside the pores. The coated samples were placed with a sample holder connected to a permeameter built in Clermont-Ferrand following Takeuchi et al. (2008). Changes from the Takeuchi et al. (2008) setup are that two of the three flow meters with low flow rates were replaced by an electronic flow meter with a range of 0–500 ml/min. The last high flow rate meter has a range of 1–16 ml/min. The permeameter allows measurement of the gas flow through

the sample at increasing steps from 0 to 10,000 ml/min. A pressure meter with a range between 0 and 200,000 Pa was used to measure the pressure drop across the sample at a given gas flow. Plotting the gas flow against the pressure drop, we solved the Forchheimer equation, which is a modified form of Darcy’s law taking into account the effects of both viscous and inertial flow during measurements (Ruth and Ma 1992; Rust and Cashman 2004). The values of the viscous permeability,  $k_1$ , obtained with the Forchheimer equation are similar to those of the apparent (Darcian) permeability,  $k_0$ , measured with Darcy’s law (Table 5). We therefore assume that inertial effects are negligible, and we use the apparent permeability data to compare with permeability data from the literature.

Vesicle size distributions and crystallinities were measured by image analysis, combining images at several different scales (Table 4). The largest vesicle and crystal populations were imaged at the sample scale using a desktop scanner, by scanning either the thin section or the sectioned sample itself. Subsequent higher magnifications ( $\times 25$ ,  $\times 100$ ,  $\times 500$ , and for one sample up to  $\times 1000$ ) were captured through scanning electron microscopy (SEM), in BSE mode, using chemical contrasting (see methodology in Leduc et al. 2015). The

**Table 1** Glass composition of the Kilian pyroclasts assessed by microprobe analysis

aay	U1_b_28	U1_b_28	U1_b_28	U1_b_28	U1_m_77	U1_m_77	U1_m_77	U1_m_77	U1_m_77	U1_b_63	U1_b_63	U1_b_63	U1_b_63	U1_b_63	U1_b_63	U1_b_63	U1_b_63
Rock type	Pumice	Pumice	Pumice	Pumice	Pumice	Pumice	Pumice	Pumice	Pumice	Pumice	Pumice	Pumice	Pumice	Pumice	Pumice	Pumice	Pumice
SiO <sub>2</sub>	66.11	65.67	65.05	64.80	65.56	68.36	66.30	66.57	65.19	66.95	66.66	65.89	66.66	66.71	66.66	66.71	67.83
TiO <sub>2</sub>	0.47	0.45	0.44	0.50	0.41	0.54	0.41	0.42	0.49	0.50	0.51	0.42	0.51	0.50	0.51	0.50	0.47
FeO	2.23	2.24	2.18	2.34	2.15	2.52	2.18	2.20	2.24	2.62	2.51	2.17	2.51	2.37	2.51	2.37	2.24
MgO	0.31	0.32	0.32	0.33	0.33	0.25	0.30	0.28	0.30	0.30	0.36	0.26	0.36	0.24	0.36	0.24	0.25
CaO	0.86	0.84	0.83	0.86	1.05	0.51	0.83	0.89	0.84	0.69	0.72	0.66	0.72	0.61	0.72	0.61	0.66
Al <sub>2</sub> O <sub>3</sub>	16.52	16.41	16.44	16.38	16.52	14.33	16.73	16.97	16.38	15.36	15.46	16.17	15.46	16.03	15.46	16.03	16.16
Na <sub>2</sub> O	6.08	5.92	5.68	5.81	5.55	5.25	6.10	6.17	5.81	5.39	5.36	5.82	5.36	5.62	5.36	5.62	5.81
BaO	0.00	0.08	0.00	0.02	0.06	0.00	0.00	0.05	0.05	0.04	0.00	0.01	0.00	0.01	0.00	0.01	0.02
Cl	0.61	0.63	0.59	0.57	0.56	0.71	0.59	0.58	0.59	0.70	0.68	0.54	0.68	0.60	0.68	0.60	0.62
P <sub>2</sub> O <sub>5</sub>	0.04	0.08	0.06	0.09	0.13	0.04	0.04	0.07	0.08	0.06	0.03	0.08	0.03	0.08	0.03	0.08	0.11
K <sub>2</sub> O	5.64	5.52	5.51	5.42	5.58	5.46	5.51	5.35	5.33	5.69	5.44	5.36	5.44	5.56	5.44	5.56	5.68
Total	98.87	98.16	97.10	97.12	97.90	97.96	98.98	99.54	97.30	98.29	97.73	97.38	97.73	98.32	97.73	98.32	99.85
Sample	U1_b_70	U1_b_70	U1_b_70	U1_b_70	U1_b_97	U1_b_97	U1_b_97	U1_b_97	U1_b_97	U1_b_97	U1_b_97	U1_b_97	U1_b_97	U1_b_97	U1_b_97	U1_b_97	U1_b_97
Rock type	Intermediate	Intermediate	Intermediate	Intermediate	Dense	Dense	Dense	Dense	Dense	Dense	Dense	Dense	Dense	Dense	Dense	Dense	Dense
SiO <sub>2</sub>	67.97	67.70	66.49	67.25	71.13	70.72	70.02	72.48	72.48	70.02	70.02	72.48	70.02	70.02	70.02	70.02	72.48
TiO <sub>2</sub>	0.51	0.54	0.54	0.57	0.79	0.59	0.80	0.74	0.74	0.80	0.80	0.74	0.80	0.80	0.80	0.80	0.74
FeO	2.48	2.43	2.32	2.38	2.19	1.96	2.29	2.39	2.39	2.29	2.29	2.39	2.29	2.39	2.29	2.39	2.39
MgO	0.19	0.32	0.34	0.29	0.06	0.11	0.10	0.06	0.06	0.10	0.06	0.06	0.10	0.06	0.06	0.06	0.06
CaO	0.91	0.70	0.59	0.65	0.27	0.20	0.24	0.20	0.20	0.24	0.20	0.20	0.24	0.20	0.20	0.20	0.20
Al <sub>2</sub> O <sub>3</sub>	15.15	15.18	15.33	15.21	12.45	12.61	12.71	11.77	11.77	12.71	12.71	11.77	12.71	12.71	12.71	12.71	11.77
Na <sub>2</sub> O	5.62	5.83	5.38	5.52	4.29	4.08	4.43	4.03	4.03	4.43	4.43	4.03	4.43	4.43	4.43	4.43	4.03
BaO	0.00	0.02	0.00	0.00	0.06	0.00	0.00	0.00	0.00	0.00	0.00	0.00	0.00	0.00	0.00	0.00	0.00
Cl	0.66	0.70	0.71	0.71	0.58	0.59	0.64	0.58	0.58	0.64	0.64	0.58	0.64	0.64	0.64	0.64	0.58
P <sub>2</sub> O <sub>5</sub>	0.00	0.04	0.09	0.07	0.03	0.06	0.02	0.08	0.08	0.02	0.02	0.08	0.02	0.02	0.02	0.02	0.08
K <sub>2</sub> O	5.55	5.59	5.54	5.51	5.44	5.60	5.81	5.41	5.41	5.81	5.81	5.41	5.81	5.81	5.81	5.81	5.41
Total	99.03	99.07	97.33	98.17	97.30	96.50	97.05	97.74	97.30	97.05	97.05	97.74	97.05	97.05	97.05	97.05	97.74

**Table 2** Bulk composition of the Kilian pyroclasts assessed by means of ICP-AES for major elements

Sample	PB11-1901-3	PB07-1110-20	PB07-1110-21	PB11-1803-6	PB11-1803-7	PB11-1803-4	C826	PB11-1803-3	PB11-1901-1	PB11-1803-2	C768C	C773B	C825	C823	C824
Rock type	Juvenile clast	Juvenile clast	Juvenile clast	Juvenile clast	Juvenile clast	Juvenile clast	Juvenile clast	Juvenile clast	Juvenile clast	Juvenile clast	Juvenile clast	Juvenile clast	Juvenile clast	Juvenile clast	Juvenile clast
SiO <sub>2</sub>	63.75	62.69	62.35	63.56	64.39	64.45	64.50	64.33	64.71	63.95	64.42	64.14	64.23	63.31	63.55
TiO <sub>2</sub>	0.55	0.57	0.58	0.53	0.54	0.55	0.52	0.53	0.53	0.53	0.49	0.51	0.53	0.53	0.53
FeO	3.18	3.37	3.38	3.10	3.18	3.18	3.12	3.02	3.11	3.12	2.98	3.12	3.21	3.26	3.20
MgO	0.50	0.55	0.52	0.52	0.53	0.55	0.49	0.50	0.52	0.51	0.48	0.53	0.54	0.49	0.52
CaO	2.02	2.05	1.95	1.94	1.98	1.93	1.93	1.96	1.95	1.94	1.96	2.09	1.96	2.02	2.01
Al <sub>2</sub> O <sub>3</sub>	18.68	19.22	19.95	18.19	17.79	17.88	18.18	17.88	17.74	18.09	18.37	18.48	18.22	19.44	19.30
Na <sub>2</sub> O	6.44	6.70	6.25	6.86	6.61	6.33	6.35	6.79	6.40	6.70	6.39	6.33	6.41	6.22	6.25
MnO	0.24	0.24	0.25	0.24	0.23	0.24	0.23	0.23	0.24	0.24	0.23	0.24	0.24	0.23	0.23
P <sub>2</sub> O <sub>5</sub>	0.18	0.43	0.58	0.15	0.17	0.16	0.16	0.18	0.19	0.15	0.15	0.15	0.16	0.17	0.17
K <sub>2</sub> O	4.45	4.18	4.20	4.92	4.57	4.71	4.51	4.59	4.62	4.77	4.52	4.41	4.49	4.32	4.24
Total	96.15	96.26	94.35	98.85	97.32	99.01	98.71	97.93	98.10	98.90	99.67	98.72	99.49	98.00	98.10

**Table 3** Grain size of the Kilian deposits

Sample	U1_base	U1_middle	U1_top	U2_base	U2_top	U3	K1	K2
$\Phi 5$	-6.01	-5.42	-4.15	-5.37	-5.32	-4.23	-5.14	-4.35
$\Phi 16$	-4.09	-5.26	-3.03	-4.35	-4.42	-3.35	-4.11	-3.46
$\Phi 25$	-3.30	-5.12	-2.26	-3.44	-4.09	-3.15	-3.30	-3.32
$\Phi 50$	-2.05	-4.05	-1.12	-2.16	-2.36	-2.07	-2.04	-2.43
$\Phi 75$	-0.23	-2.41	0.53	-0.21	-1.01	-0.32	-0.14	-1.38
$\Phi 84$	0.65	-1.50	0.93	0.83	-0.13	0.57	0.79	-1.06
$\Phi 95$	2.63	0.65	2.98	3.63	1.88	2.87	2.81	0.81
$Md\phi$	-2.05	-4.05	-1.12	-2.16	-2.36	-2.07	-2.04	-2.43
$\sigma\phi$	2.37	1.88	1.98	2.59	2.14	1.96	2.45	1.20
SK	0.14	0.36	0.04	0.15	0.04	0.34	0.15	0.14
K	0.82	0.61	0.80	0.74	0.68	0.81	0.62	1.15
Lapilli	51.74	83.94	33.71	55.33	61.10	52.75	51.30	71.48
Coarse ash	46.94	15.03	65.43	41.89	37.70	44.57	46.84	27.30
Fine ash	1.32	1.03	0.87	2.78	1.21	2.68	1.87	1.21

$\Phi 5$  up to  $\Phi 95$  percentile,  $Md\phi$  mean diameter,  $\sigma\phi$  sorting, SK skewness, K kurtosis calculated following Inman (1952), Lapilli percentage of fragments >2 mm in diameter, Coarse ash percentage of fragments <2 and >0.064 mm in diameter, Fine ash percentage of fragments <0.064

images were treated in the Adobe Photoshop software and used as inputs into the Matlab-based “FOAMS” program (Shea et al. 2010a) to obtain vesicle size distributions (VSDs), vesicle number densities (N<sub>vs</sub>), and crystallinities. Details of the analysis strategy, as well as the stereological assumptions adopted, can be found in Shea et al. (2010a). For all thin sections, the smallest size limit,  $L_{\min}$ , was controlled by the image acquisition and fixed at 5 pixels in diameter (1.5  $\mu\text{m}$ ). This led to an underestimation of the number of small vesicles in all the thin sections, except for clast U1\_b\_96 (Table 4), for which we used a higher magnification ( $\times 1000$ ) due to the presence of nanometric vesicles, for which  $L_{\min}$  is about 0.5  $\mu\text{m}$ .

## Results

### Section description

The Coupe des Muletiers sample section is 5 m thick and is located 1 km NNE of Kilian crater (Fig. 1b). The section is subdivided into five units, U1, U2, U3, K1, and K2, based on grading characteristics and the distribution of bomb sag horizons (Fig. 3a). The two lowermost units (U1 and U2) vary locally in thickness and contain felled carbonized logs. The uppermost three units (U3, K1, and K2) have more constant thicknesses at the outcrop scale. Bomb sags are present at the base of each unit.

**Unit U1** Basal unit U1 has three layers. The first layer (U1\_base, Fig. 3) is composed of poorly sorted, normally graded coarse lapilli and bombs to coarse ash, with an

irregular thickness up to 50 cm. The coarse-grained base is characterized by angular lapilli, bombs, and blocks, in a pink ash matrix. The fine-grained top, yellow-brown in color, contains scattered coarse lapilli and charcoal. The grain size distribution of the layer is asymmetrical with a tail toward the fine portion (positively skewed) and broad (platykurtic) (Fig. 3b and Table 3). The second layer (U1\_middle, Fig. 3) is a normally graded, well-sorted, coarse layer of bombs and blocks fining upward to lapilli size. The irregular thickness ranges from 50 to 100 cm. Bread-crust bombs are present. The grain size distribution is positively skewed (Fig. 3b and Table 3). The uppermost layer (U1\_top, Fig. 3) is a darker, fine-rich, and well-sorted layer up to 75 cm in thickness. Its grain size distribution is broad and nearly symmetrical (Fig. 3b).

**Unit U2** U2 is composed of a thick, coarse-grained lower layer (U2\_base, Fig. 3b) and a thinner, coarse-ash upper layer (U2\_top). It varies in thickness locally from 10 cm to 2 m. Both layers are poorly sorted and characterized by broad grain size distributions, positively skewed to nearly symmetrical. Bread-crust bombs are present in layer U2\_base.

**Unit U3** U3 is a thinner layer of well-sorted lapilli and coarse ash, with a thickness up to 40 cm. The grain size distribution is positively skewed and broad (Fig. 3b and Table 3).

**Units K1 and K2** Unit K1 is up to 35 cm in thickness and is composed of coarse lapilli and blocks of trachyte, basalt, and granite in a yellowish matrix; the grain size distribution is broad and positively skewed (Fig. 3b and Table 3). Unit K2 is up to 1 m thick and is characterized by an oxidized orange



**Table 4** Summary of the textural features of the juvenile clasts from Kilian deposits

Sample	Unit	$\rho$ (kg m <sup>-3</sup> )	$\Phi$ (vol%)	$\bar{x}$ (vol%)	C	N <sub>im</sub>	N <sub>ves</sub>	N <sub>ctx</sub>	Ctx <sub>tot</sub> (%)	Pheno (%)	Microclitics (%)	N <sub>v</sub> (mm <sup>-3</sup> )	N <sub>v</sub> <sup>corr</sup> (mm <sup>-3</sup> )	N <sub>v</sub> <sup>iso</sup>	D	N <sub>oxides</sub> (mm <sup>-3</sup> )
U1_b_28	U1_base	620	77	2.1	97.4	16	1330	278	8.5	5.0	3.5	4.37E+05	1.63E+06	2.45E+05	3.50	3.12E+05
U1_b_63	U1_base	1100	57	3.6	94.1	16	3146	773	17.3	3.2	14.1	1.39E+06	3.07E+06	7.25E+05	4.16	4.35E+05
U1_b_70	U1_base	1550	41	3.7	91.8	16	3683	537	23.0	8.0	15.0	2.20E+06	3.82E+06	1.63E+06	4.00	7.03E+06
U1_b_96	U1_base	2150	19	1.2	94.0	10	8885	960	47.0	9.0	38.0	9.80E+07	1.32E+08	4.55E+07	3.88	2.80E+06
U1_b_97	U1_base	2280	14	2.4	85.6	16	934	465	38.0	8.0	30.0	1.39E+06	3.17E+06	1.17E+06	2.13(9.11)	2.80E+06
U1_m_77	U1_middle	670	75	4.5	94.3	16	1903	478	11.0	4.0	7.0	8.90E+05	2.70E+06	6.43E+05	3.61	3.61E+06
U2_b_29	U2_base	1180	55	1.0	98.2	15	2039	405	23.9	6.0	17.9	3.23E+06	3.43E+06	1.06E+06	3.46	3.46E+06
K1_b_61	K1_base	2170	18	1.2	93.8	15	5600	280	27.0	7.0	20.0	5.00E+06	5.37E+06	1.13E+06	2.66(5.00)	5.99E+05
K1_t_6	K1_top	790	70	1.9	97.4	15	1200	367	13.0	3.6	9.4	1.07E+06	1.11E+06	3.95E+05	3.70	3.70E+06
K1_t_63	K1_top	1290	51	2.3	95.7	15	2239	401	26.5	6.9	19.7	1.93E+06	2.08E+06	6.86E+05	3.96	3.61E+05
K1_t_64	K1_top	2290	13	0.4	97.1	15	3820	340	55.0	7.0	48.0	4.07E+06	4.38E+06	1.95E+06	3.73	1.97E+06

The table shows the following: for each sample: sample name (sample), deposit unit (unit), measured density ( $\rho$ ), porosity obtained combining bulk and solid densities ( $\Phi$ ), measured isolated porosity ( $\bar{x}$ ), pore connectivity in percentage (C), number of images processed for each sample (N<sub>im</sub>), number of vesicle and crystal analyzed for each sample, respectively (N<sub>v</sub>, N<sub>ctx</sub>), percentage of total crystals (Ctx<sub>tot</sub>), percentage of phenocrysts (Pheno), percentage of microclitics (microclitic), total volumetric number density of vesicles referenced to whole clast (N<sub>v</sub>), total volumetric number density of vesicles referenced to melt only (N<sub>v</sub><sup>corr</sup>), total volumetric number density of isolated vesicles (N<sub>v</sub><sup>iso</sup>), fractal dimension (D), and total volumetric number density of oxides (N<sub>oxides</sub>)

matrix of hydrothermally altered ash with scattered angular coarse lapilli, blocks, and bombs. The grain size distribution is narrow and positively skewed (Fig. 3b and Table 3). K1 and K2 correlate with two prominent layers in the deposit at the summit of the Puy de Dôme, where they are underlain by numerous bomb sags.

There is no evidence in the sequence of significant pauses in eruptive activity between the eruption of units U1, U2, U3, and K1. The abundance of hydrothermally altered material in unit K2 may record a preceding pause long enough for significant fumarolic activity at the crater.

### Componentry

Juvenile particles (hereafter termed pyroclasts) in the deposit have variable sizes, shapes, colors, and densities (porosities). We use the term “pumice” for pyroclasts with porosities  $\Phi > 40\%$  and “dense pyroclasts” for those with  $\Phi \leq 40\%$ , although the transition between them is gradual. These pyroclasts are trachytes (62–64 wt% SiO<sub>2</sub>, Tables 1 and 2) and contain <10 vol% phenocrysts of Ti-amphibole, biotite, and oligoclase set in a fine-grained groundmass; apatite, zircon, and titanomagnetite are also present (Boivin et al. 2015). The bulk composition is independent of porosity (Table 2), while the glass chemistry reflects a higher crystallinity in the dense pyroclasts (Table 1).

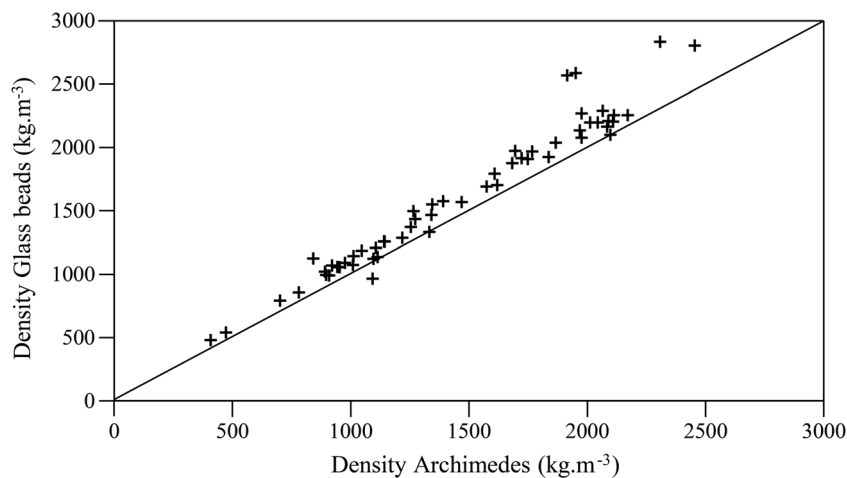
The pumices are rounded to sub-rounded, have smooth surfaces, and are beige-gray in color (Fig. 6a). Dense pyroclasts have more angular shapes, with a quenched, dense, vesicle-poor, and occasionally breadcrusted rind, and are dark gray to black in color (Fig. 6b). Some rare pyroclasts are texturally brecciated or banded and contain small included fragments of other pyroclasts (either vesicular or dense) and accidental debris (Fig. 6c); these are particularly abundant in unit U1. They most likely represent tuffisites that are remnants of ash-filling veins in the host magma (e.g., Castro et al. 2012; Saubin et al. 2016).

Non-juvenile clasts include fragments of pre-existing lava/scoria and granitic basement. Units U2 and U3 are poorer in non-juvenile fragments and in dense juvenile fragments than units U1, K1, and K2 (Fig. 3c).

### Clast density and porosity

The bulk densities of the pyroclasts range from 330 to 2630 kg m<sup>-3</sup>, corresponding to porosities of 0 to 82% (Fig. 3d and Table 4). Units U1, K1, and K2 are characterized by polymodal density distributions, with a dominant peak for pumice at ~1000 kg m<sup>-3</sup> and a second main peak, for the dense fragments at ~2000 kg m<sup>-3</sup>. In contrast, units U2 and U3 show a narrow, unimodal density distribution with a peak at intermediate density value (1200–1300 kg m<sup>-3</sup>).

**Fig. 4** Comparison between density data of the juvenile clasts derived from clast immersion in 200–400- $\mu\text{m}$  diameter glass beads based on a method described by Nakamura et al. (2008) and Silva (2008) and those derived by the water immersion (Archimede's) method (Houghton and Wilson 1989). The mean error of the measurements is reported in the text



### Pore connectivity and permeability

Figure 5 shows the pore connectivity and permeability relationships versus bulk porosity for the dense rocks and the pumices. Note that for the connectivity, the division of the clasts into dense clasts and pumices was based on macroscopic observations, so they do not correspond exactly to the porosity threshold at  $\Phi = 40\%$  discussed earlier. Most of the connectivities,  $C$ , are between  $0.75 < C < 1$  (Fig. 5a and Table 5), with only a few data points with lower connectivity. A few data are also observed with  $C > 1$ , which is not physical and is related to the error on the measurement. We consider these data as highly connected. The range of connectivity for dense rocks broadens constantly while the porosity decreases, from  $C \sim 1$  at a porosity  $\Phi = 60\%$  to  $C = [0.5 \text{ to } 1]$  at  $\Phi = 10\%$ . Pumices form a cluster and no clear trend is distinguished.

Apparent permeability values  $k_0$  range from  $10^{-16}$  to  $10^{-11} \text{ m}^2$  (Table 5). A plot of porosity  $\Phi$  versus apparent permeability  $k_0$  shows a scattered increase of  $k_0$  with  $\Phi$ , for  $\Phi = 10\text{--}40\%$ ; in contrast, pumices with  $\Phi = 40\text{--}70\%$  display an approximately constant range of high values ( $10^{-13}$  to  $10^{-11} \text{ m}^2$ , Fig. 5b). Some dense juvenile clasts are more

permeable than highly vesicular ones. Maximum permeability is achieved in the Kilian trachyte at porosities of 35–40 vol%.

### Microscopic textural features of the Kilian trachytes

Vesicles within the Kilian pyroclasts cover a broad range of sizes, from  $10^{-4}$  to  $10^1 \text{ mm}$ . Two distinct populations can be distinguished from microscopic observations: “large vesicles”  $>600 \mu\text{m}$  in diameter and “small vesicles”  $<600 \mu\text{m}$  in diameter. One dense clast (U1\_b\_96, Table 4,  $\rho = 2150 \text{ kg m}^{-3}$ ) has a large fraction of very small vesicles, the smallest measuring  $<0.1 \mu\text{m}$  in diameter.

Large vesicles occur mostly in pumices and are rare in dense pyroclasts. They form rounded voids surrounding phenocrysts or angular fractures within phenocrysts. Small vesicles in pumices have rounded to elongated shapes and smooth walls (Fig. 6d). The mean size of this small vesicle population decreases and the elongation increases as clast density increases in the pumice population. Small vesicles are organized radially along interstices between microlites, being mostly interconnected in pumices, and locally stretched either parallel

**Fig. 5** **a** Pore connectivity versus bulk porosity for dense clasts (black crosses) and pumices (red squares). **b** Apparent permeability versus bulk porosity for dense clasts and pumices

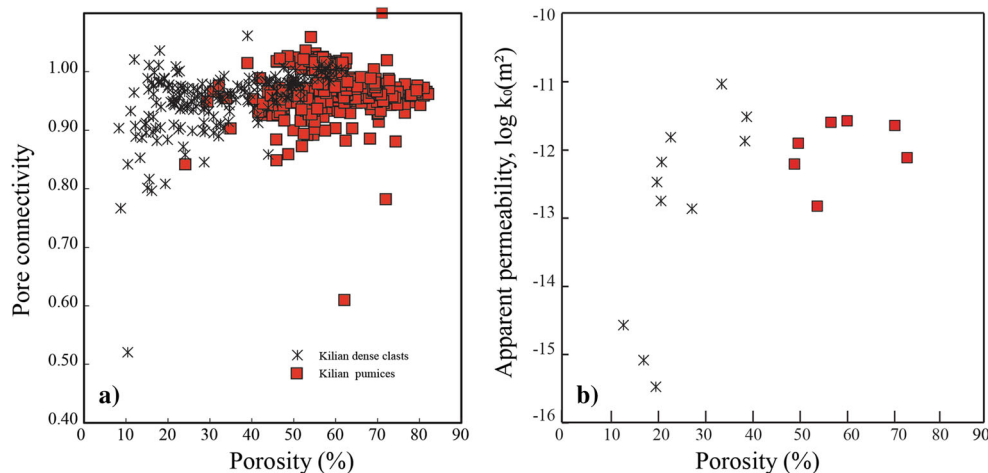


**Table 5** Summary of the permeability analysis on 18 juvenile clasts of a broad range of density

Sample	Unit	$\Phi_c$	$\Phi_{tot}$	$\Phi_{iso}$	$\Phi_{Archimedes}$	Density ( $\text{kg m}^{-3}$ )	$C$	$k_0$ (apparent)	$k_1$ (Darcian or viscous)	$k_2$ (non-Darcian or inertial)
U1_b_103	U1_base	21	22	1	21	2086	0.94	1.8E-13	1.7E-13	1.8E-09
U1_b_110	U1_base	16	17	2	17	2191	0.90	7.2E-16	4.5E-16	–
U1_b_63	U1_base	56	57	1	57	1135	0.98	2.5E-12	4.1E-12	1.9E-07
U1_b_71	U1_base	47	50	3	50	1320	0.93	1.3E-12	2.1E-12	8.5E-08
U1_m_2	U1_middle	19	20	1	21	2096	0.95	3.9E-16	4.4E-16	–
U1_m_3	U1_middle	43	44	1	49	1341	0.98	6.2E-13	7.5E-13	2.3E-06
U1_m_4	U1_middle	26	27	1	28	1914	0.96	1.4E-13	2.9E-13	1.4E-08
U1_t_6	U1_middle	–	–	–	23	2033	–	1.6E-12	1.5E-13	4.1E-09
U2_b_29	U2_base	54	55	1	60	1045	0.98	2.7E-12	2.0E-12	3.2E-07
K1_b_3	K1_base	28	28	0	34	1748	1.00	8.7E-12	1.5E-11	4.0E-07
K1_t_1	K1_top	68	70	2	73	713	0.97	7.7E-13	9.1E-13	4.0E-08
K1_t_64	K1_top	13	13	0	13	2297	1.00	2.7E-15	2.0E-15	1.2E-12
K1_t_63	K1_top	49	51	2	54	1214	0.96	1.5E-13	1.7E-13	1.2E-08
K2 Mul 1	K2	67	68	1	70	781	0.99	2.3E-12	2.5E-12	9.8E-08
K2 Mul 3	K2	30	32	2	39	1608	0.94	3.0E-12	3.1E-12	2.3E-08
K2 Mul 4	K2	34	36	2	39	1618	0.94	1.4E-12	1.5E-12	9.1E-08
K2Mul5	K2	16	16	0	21	2086	1.00	6.6E-13	9.2E-13	1.1E-08
K2_3	K2	16	17	1	20	2109	0.94	3.4E-13	5.2E-13	2.7E-09

Connected ( $\Phi_c$ ), bulk (characterized with the glass bead method;  $\Phi_{tot}$ ), Archimedes bulk porosity ( $\Phi_{Archimedes}$ ) and isolated ( $\Phi_{iso}$ ) porosity, density, pore connectivity in fraction ( $C$ ), apparent permeability ( $k_0$ ), viscous permeability ( $k_1$ ), and inertial permeability ( $k_2$ ). The porosity used in the  $k$  vs.  $\Phi$  plot is the Archimedes-derived bulk vesicularity

or perpendicular to the microlite alignment in denser pumices. Evidence of vesicle coalescence, as previously discussed by Klug and Cashman (1996), includes (1) melt film flattening, thinning, wrinkling, failure, and retraction at the boundaries between adjacent coalescing vesicles (Fig. 6d); (2) coalescence of small vesicles into a central, larger vesicle; and (3) progression radially out from a central bubble, with surrounding bubbles deforming and eventually coalescing into it. Only vesicles smaller than 10  $\mu\text{m}$  are well rounded and do not show signs of coalescence, suggesting that they are isolated. In dense pyroclasts, the small population can be further separated into very small vesicles that are rounded and isolated (Fig. 6e) or coalesced (Fig. 6h, f), and larger vesicles that have rounded to angular shapes. These latter are strongly influenced by the presence of microlites, and form clusters of coalesced vesicles (Fig. 6e, h, i). Additionally, most small vesicles in all samples are attached to Fe-Ti oxide grains, suggesting that they nucleated heterogeneously on that mineral phase (Fig. 6e, i). There is no obvious evidence of vesicle anisotropy in the dense clasts. The high pore connectivity in the pumices results from bubble growth

and coalescence; in the dense pyroclasts, the high interconnectivity can be explained by bubble coalescence enhanced by the presence of crystals and extensive cracking (Fig. 6e).

The microlite content is higher in the denser clasts (Fig. 6e–g). Microfractures in microlites occur in all the samples and are frequently continuous into the groundmass, connecting coalesced vesicles and increasing pore connectivity (Fig. 6e). SEM observations reveal that most of the microfractures in microlites are perpendicular to their length, although cracks either parallel or with an angle of 45° to the long axis are also found.

### Vesicle size distributions

Vesicle volume distributions are shown on plots of volumetric percentage versus vesicle diameter ( $L$  in mm, expressed as the diameter of a sphere of the same volume, Fig. 7). The data from both pumices and dense clasts span a large range of vesicle sizes, but distributions are shifted toward smaller sizes for the dense clasts.

The distributions in the most vesicular (>70%) pumices are bimodal, with a dominant mode of small vesicles and a

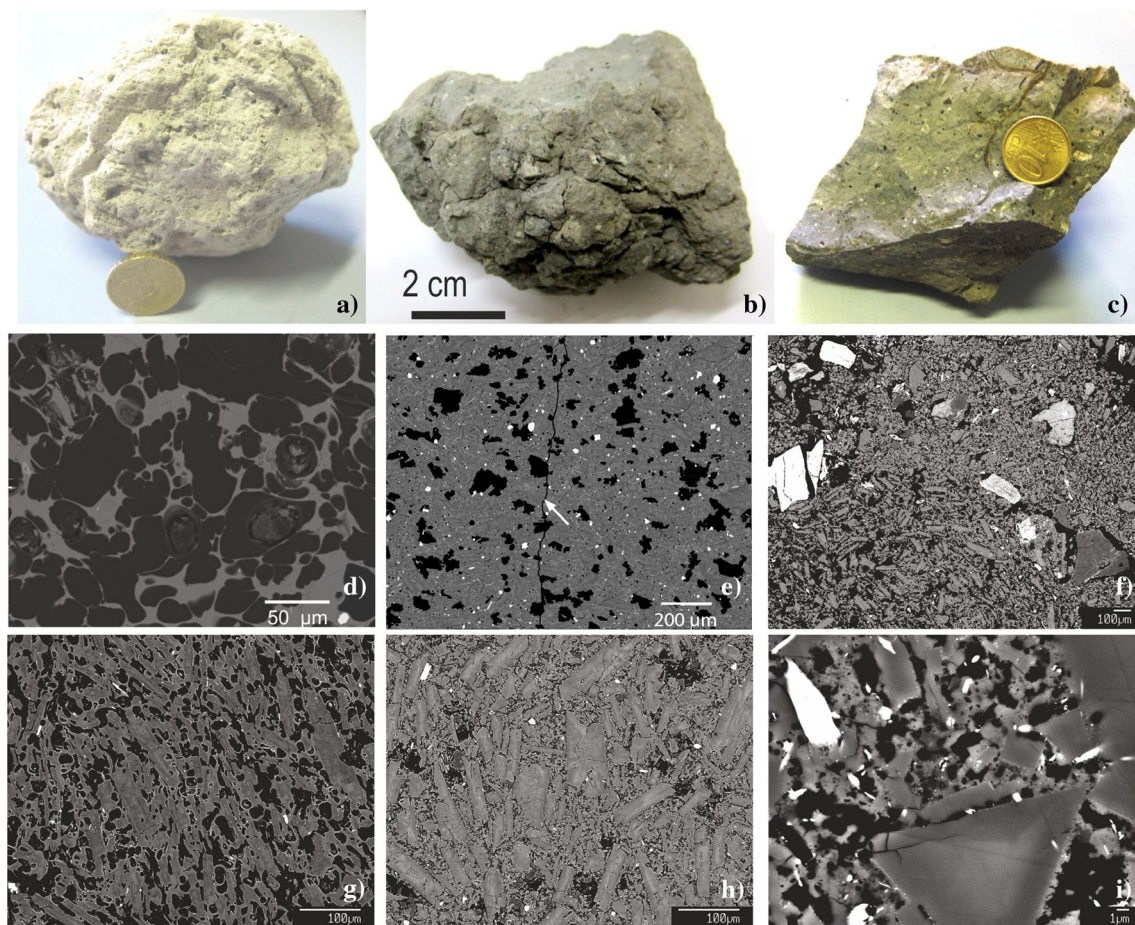


**Fig. 6** Juvenile fragments of Kilian deposits. **a** Pumice fragment. **b** Dense fragment. **c** Brecciated fragment. SEM images of textures in the Kilian pyroclasts. **d** A pumice (U1\_m\_77). **e** Dense clast U1\_b\_97. The *white arrow* shows a microcrack connecting clusters of vesicles. **f** Brecciated texture formed by the alternation of dense and more

vesiculated portions (U1\_b). **g** Intermediate texture with elongated and slightly angular vesicles (U1\_b\_70). **h** Dense clast U1\_b\_96 rich in very small vesicles. **i** Magnification of **h**, showing association of small vesicles and Fe-Ti oxides

subordinate mode of large vesicles. For pumices with intermediate porosities (50–55%), the large population either forms a tail on the small population or is absent (e.g., clast U1\_b\_63). The vesicle volume distributions of the dense clasts are characterized by unimodal distributions, and large vesicles are almost absent. Two types of distributions are observed in these dense clasts (Fig. 7): clasts U1\_b\_96 and K1\_t\_64 have modes at small  $L$  and positive skewness; clasts U1\_b\_97 and K1\_b\_61 have modes at larger  $L$  and negative skewness.

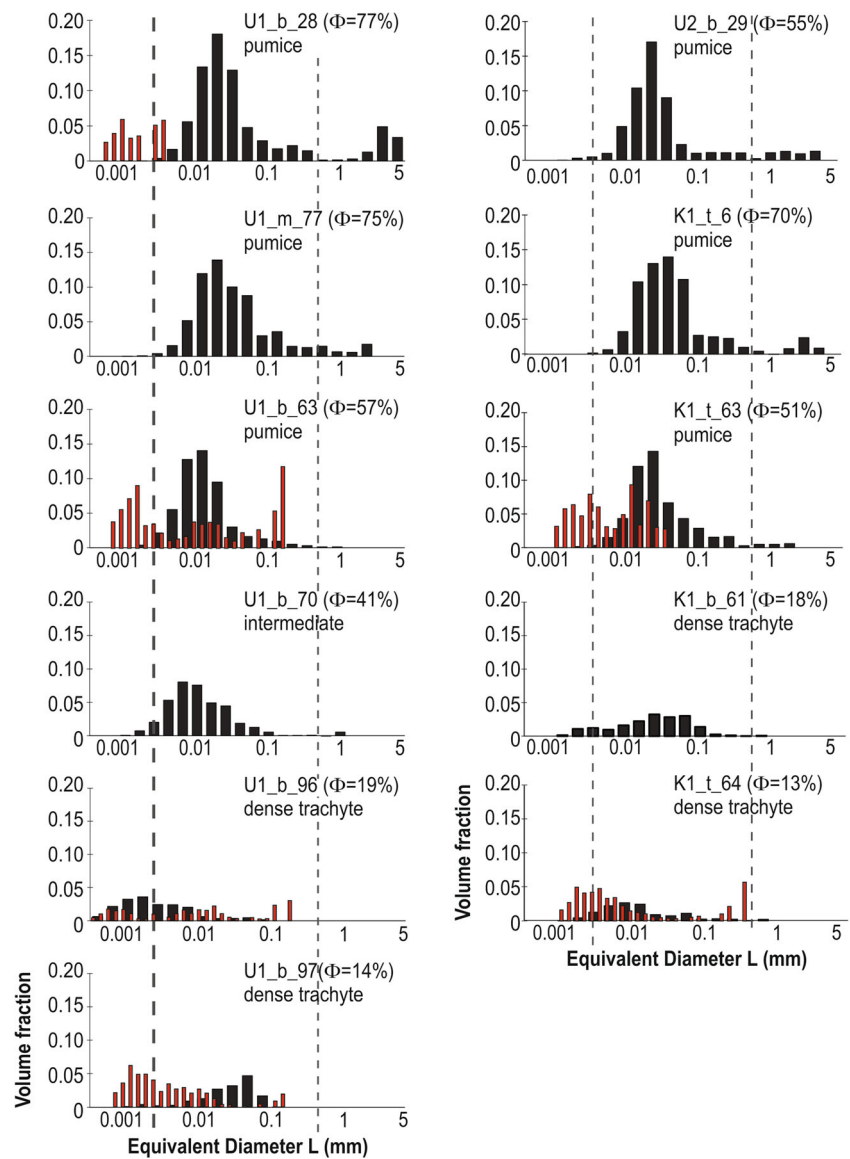
The cumulative number density distributions for all samples show distinct trends for pumices and dense pyroclasts (Fig. 8). Pumices have distributions characterized by similar curves, with slope breaks at  $L \approx 10\text{--}20 \mu\text{m}$  shown by the solid vertical line in Fig. 8a. For a vesicle diameter larger than  $10\text{--}20 \mu\text{m}$ , the distribution defines a linear trend that obeys a power law behavior (PL, Fig. 8, see also similar trends in Giachetti et al. 2010). Measuring the slope of this linear trend enables us to obtain the fractal dimension  $D$  for each clast (Table 4). Pumices have fractal dimensions of 3.45 and 4.20,

with an average of 3.73. Distributions of the smallest vesicles ( $<10\text{--}20 \mu\text{m}$ ) deviate from this power law distribution and define an exponential (EXP, Fig. 8) trend.

Cumulative number density distributions for the dense pyroclasts do not fall on a single trend (Fig. 8a). We thus represented the individual distribution for each dense clast (Fig. 8b–e). Dense pyroclasts U1\_b\_96 and K1\_t\_64 both exhibit similar power law trends with high fractal dimensions ( $D = 3.88$  and  $3.73$ , respectively) for vesicles larger than  $1\text{--}5 \mu\text{m}$ ; the trends for smaller vesicles are exponential. In contrast, the break in slope for dense clasts U1\_b\_97 and K1\_b\_61 lies at a significantly higher value of  $L$  ( $\sim 50 \mu\text{m}$ ). For vesicles with  $L < 50 \mu\text{m}$ , distributions define a power law with low fractal dimensions ( $D1 = 2.13$  and  $2.66$ , respectively), whereas larger ( $>50 \mu\text{m}$ ) vesicles follow a power law but with extremely high values of  $D$  ( $D2 = 9.11$  and  $5.00$ , respectively).

The  $N_v$ s of dense pyroclasts and pumices fall within a limited range ( $0.4\text{--}5 \times 10^6 \text{mm}^{-3}$ , Table 4). The only exception is the dense clast U1\_b\_96, which has a much higher  $N_v$ ,

**Fig. 7** Vesicle (*black*) and Fe-Ti oxides (*red*) volume distributions in Kilian pyroclasts



( $\sim 10^8 \text{ mm}^{-3}$ , Table 4). These number densities (Table 4) were corrected for crystallinity and thus correspond to the number density of the melt.

**Oxide microlite size distribution**

Our measurements of crystal size distribution focused solely on Fe-Ti oxide microlites, the objective being to check whether the oxides could have acted as nuclei for heterogeneous nucleation of the very small vesicles. This was possible only in clasts in which oxides stood out with sufficient contrast on BSE images. The oxide size distributions are overlain on the VSD plots of Fig. 7. Oxide volume fractions have been multiplied by 100 for pumices and 10 for dense clasts to allow comparison. In dense clasts, the ranges of oxide sizes correspond to the ranges of vesicle sizes, whereas vesicles are shifted to larger size in pumices.

The number densities of Fe-Ti oxides,  $N_{\text{oxides}}$ , measured with FOAMS is lower than, or of the same order of magnitude as,  $N_v$  (Table 4). However, we underestimate their number density due to (i) the lower intersection probability for oxide microlites or nanolites compared to larger vesicles (Sahagian and Proussevitch 1998) and (ii) the minimum size of objects counted by FOAMS (5 pixels). A higher magnification would have been necessary for each clast to take into account more oxides. Finally, despite the high spatial resolution of most SEMs, there are potentially numerous nanometer-sized oxides that could be difficult to image (e.g., Mujin and Nakamura 2014).  $N_{\text{oxides}}$  in clast U1\_b\_96 is significantly higher than for other Kilian clasts, with nanometric oxides revealed by SEM images. However, despite the previously mentioned discrepancies, a clear positive correlation exists between  $N_{\text{oxides}}$  and  $N_v$ , both parameters being lowest in (microlite poor) pumices and highest in (microlite rich) dense clasts (Fig. 9a).

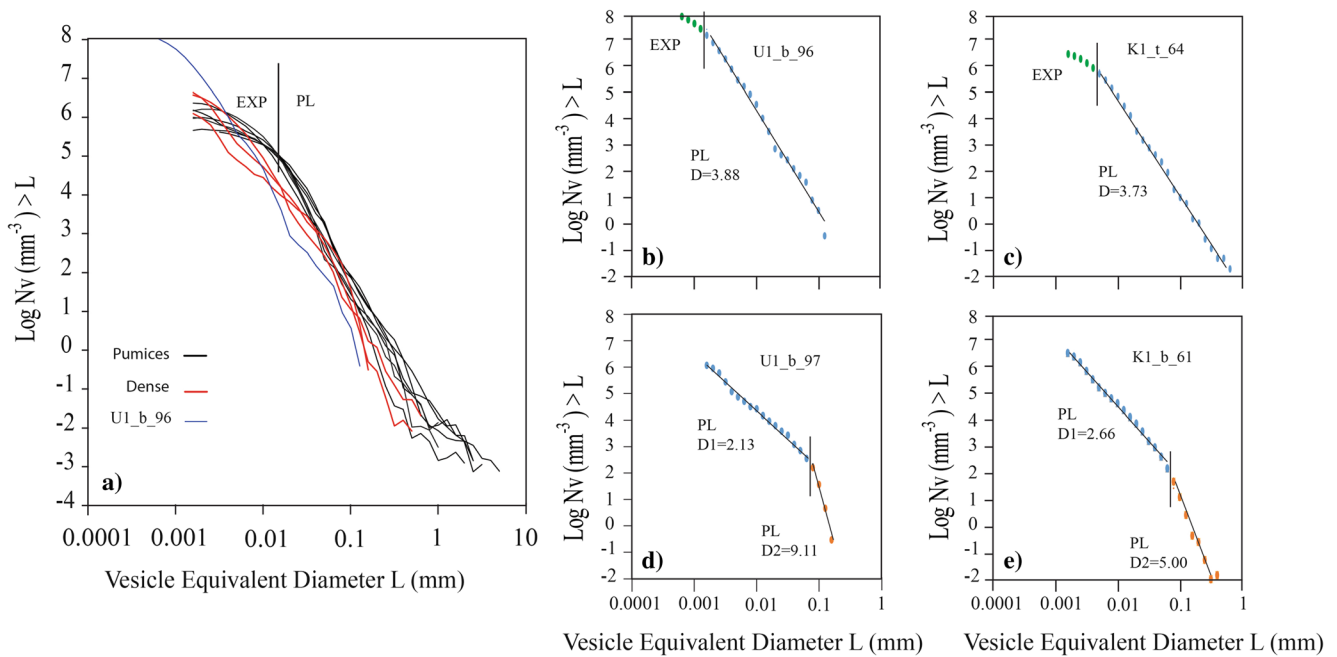


**Fig. 8** Vesicle equivalent diameter ( $L$ ) vs cumulative number density for **a** all the samples and **b–e** specific samples. Full explanation in the text

**Calculation of decompression rates**

Using the calculated  $N_v$ s, we can estimate the decompression rates using the decompression rate meter of Toramaru (2006) expressed as follows:

$$N_v \approx 34 X_{SAT} \left( \frac{16\pi\sigma_{MB}^3}{3k_B T P_{SAT}^2} \right)^{-2} \left( \frac{V_M P_{SAT}}{k_B T} \right)^{-1/4} \left( \frac{P_{SAT}^2 k_B T X_{SAT} D_{H_2O}^{H_2O}}{4\sigma_{MB}^2 |dP/dt|} \right)^{-3/2}, \tag{1}$$

where  $X_{SAT}$  is the water concentration at the initial saturation conditions (number of  $H_2O$  molecules per volume melt),  $P_{SAT}$  the initial pressure at saturation,  $D_{H_2O}$  is the diffusivity of  $H_2O$  in the melt,  $V_M$  is the volume of a water molecule in the melt,  $\sigma_{MB}$  is the melt-bubble interfacial energy (=surface tension for liquids, typically expressed in N/m),  $k_B$  is the Boltzmann constant, and  $T$  is the temperature. Rather than choosing the high initial storage pressures associated with phenocryst phase equilibria (Martel et al. 2013), we opted for an initial pressure  $P_{SAT} = 50$  MPa consistent with shallow storage conditions preceding vulcanian eruptions (assuming volatile-rich magma stalled for a given period prior to and during plug/dome formation, as shown by the microlite crystallization). These pressure conditions are similar to those inferred by Burgisser et al. (2010, 2011) for 1997 Soufriere Hills magmas based on groundmass glass  $H_2O$  measurements. We used the inferred magma temperature of  $T = 775$  °C (Martel et al. 2013). Water concentration at the initial pressure was calculated based on  $H_2O$  solubility in trachyte melt from Di Matteo et al. (2004) and  $H_2O$  diffusivity estimated by extrapolating the model of Fanara et al. (2013) to lower temperatures. Values of surface tension used were  $\sigma \sim 0.025$  N/m, which assumes bubbles

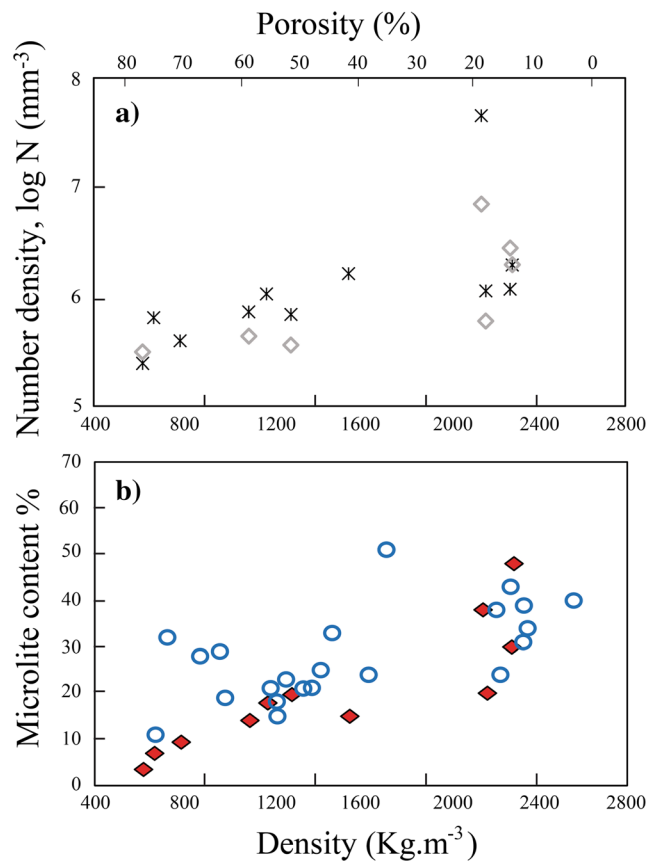


**Fig. 9** **a** Number densities of isolated vesicles (black crosses) and of oxides (gray open diamonds). **b** Melt microlite content as a function of clast density in Kilian pyroclasts (red diamonds) and in Soufrière Hills pyroclasts (blue open circles; Clarke et al. 2007)

nucleated heterogeneously on Fe-Ti oxides (Cluzel et al. 2008). The decompression rates obtained range between 4.0 and 11.5 MPa s<sup>-1</sup> (Table 6). We note that using surface tension values for homogeneous nucleation resulted in unrealistic values of decompression rates ( $\geq 100$  MPa s<sup>-1</sup>), supporting the notion that bubbles within Kilian magmas probably nucleated heterogeneously. The sample U\_b\_96 was excluded from this calculation, because of the very high  $N_v$ .

## Discussion

### Mode of tephra emplacement

The Kilian deposit is interpreted as the product of at least five explosions, each unit being the product of a single explosion (i.e., a single continuous eruptive pulse). The presence of bomb sags at the base of each unit records ballistic showers accompanying the onset of each explosion. The two basal units (U1 and U2) have features indicative of emplacement by pyroclastic density currents and include poor sorting, local variations in thickness, and the presence of felled carbonized logs. The absence of U1 and U2 at the summit of the Puy de Dôme is consistent with the inability of the density currents to surmount the high topography. In contrast, the topmost three units (U3, K1, and K2) have features consistent with a larger

component of fallout, including better sorting, relatively constant thickness at the outcrop scale, and (in the cases of K1 and K2) presence atop the Puy de Dôme. The decrease in thickness and grain size from the base to the top of the whole sequence suggests a series of explosions of decreasing eruptive intensity with time, with the first two involving a larger component of lateral emplacement than the last three, as shown by their distribution (Fig. 2) and variations in thickness (Fig. 3a). However, syneruptive gravitational slide deposits formed during late ash fall episodes (K1-K2), with partial reworking of U1 and older pyroclastic deposits, complicated the distribution of the whole sequence of the Kilian deposits (Fig. 2).

### Nature of the explosions and origin of the dense pyroclasts

The explosions generated pyroclasts with a wide range of densities. Density distributions for units U1, K1, and K2 (combined in Fig. 10) are wide and bimodal, with a low-density mode around 800–1100 kg/m<sup>3</sup> and a high-density mode around at 2000–2500 kg/m<sup>3</sup>. In contrast, units U2 and U3 are each unimodal with a mode at 1200 kg m<sup>-3</sup>.

The trachytic pumice and dense trachytic clasts are both considered to be juvenile since their chemical compositions (Table 2) and phenocryst associations are identical, and they grade texturally into one another (Fig. 6 and Tables 1 and 2).

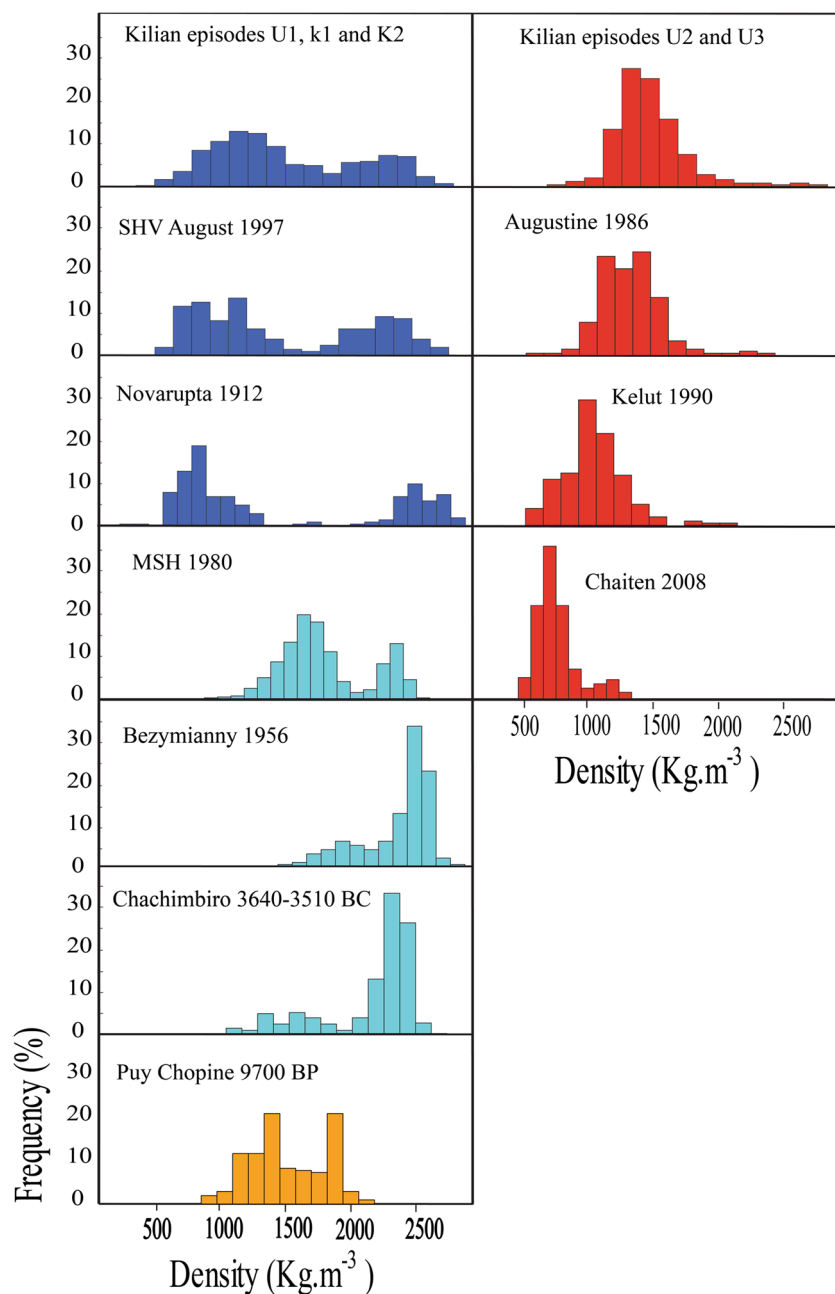
**Table 6** Calculated decompression rates for the Kilian products for heterogeneous and homogeneous nucleation

Conditions		$T = 775$ °C $P_i = 50$ MPa Heterogeneous nucleation ( $\sigma_{\text{het}} = 0.025$ N m <sup>-1</sup> )	$T = 775$ °C $P_i = 50$ MPa Homogeneous nucleation ( $\sigma_{\text{hom}} = 0.065$ N m <sup>-1</sup> )
Sample	Unit	dP/dt (MPa s <sup>-1</sup> )	dP/dt (MPa s <sup>-1</sup> )
U1_b_28	U1_base	5.19	35.07
U1_b_63	U1_base	7.91	53.49
U1_b_70	U1_base	9.15	61.88
U1_b_96	U1_base	n/a <sup>a</sup>	n/a <sup>a</sup>
U1_b_97	U1_base	8.08	54.64
U1_m_77	U1_middle	7.26	49.10
U2_b_29	U2_base	8.52	57.59
K1_b_61	K1_base	11.49	77.65
K1_t_6	K1_top	4.02	27.15
K1_t_63	K1_top	6.10	41.26
K1_t_64	K1_top	10.03	67.79

Model assumptions are explained in the text (surface tension)

<sup>a</sup> Vesicles in sample are partially unrelated to bubble nucleation

**Fig. 10** Total density distribution histograms for Kilian, Soufrière Hills Montserrat (SHV) August 1997 (Belousov et al. 2007), Novarupta 1912 (Adams et al. 2006), Mount St Helens (MSH) 1980 (Hoblitt and Harmon 1993), Bezymianny (BE) 1956 (Belousov et al. 2007), Kelut 1990 (Mueller et al. 2011), Augustine 1986 (Mueller et al. 2011), Chachimbiro (Bernard et al. 2015), Puy Chopine (Boudon et al. 2015), and Chaiten 2008 (Alfano et al. 2012)



From the most vesicular to the least vesicular clasts, the microlite content increases (Figs. 7 and 9b and Table 1), and the large vesicle population present in pumices disappears (Fig. 7). The high microlite content of the densest clasts, and the anti-correlation between porosity and microlite content (Fig. 9b), is consistent with derivation of the dense trachytic clasts by decompression-induced outgassing of the gas-rich magma. Rare breadcrusting (Fig. 6b) on some of the dense clasts also attests to their magmatic origin.

Pyroclasts with a wide range of densities are generated in explosive eruptions by several factors (see Gurioli et al. 2015 for a review); however, two main mechanisms have been proposed for the vulcanian dense clasts: (1) vertical eruption of

gas-charged magma from beneath an outgassed magmatic plug or lava dome (Morrissey and Mastin 2000; Formenti and Druitt 2003; Houghton et al. 2004; Adams et al. 2006; Giachetti et al. 2010) or (2) lateral decompression of a dome/cryptodome containing an outgassed margin and less outgassed interior (Hoblitt and Harmon 1993; Belousov et al. 2007; Neill et al. 2010; Bernard et al. 2015; Boudon et al. 2015). Comparison of the Kilian pyroclast density distributions with published data from other eruptions (Fig. 10) shows that pyroclasts in units U1, K1, and K2 resemble those from the 1997 vulcanian explosions of Soufrière Hills Volcano, Montserrat (Formenti and Druitt 2003; Giachetti et al. 2010), and from episode IV of the 1912 Novarupta



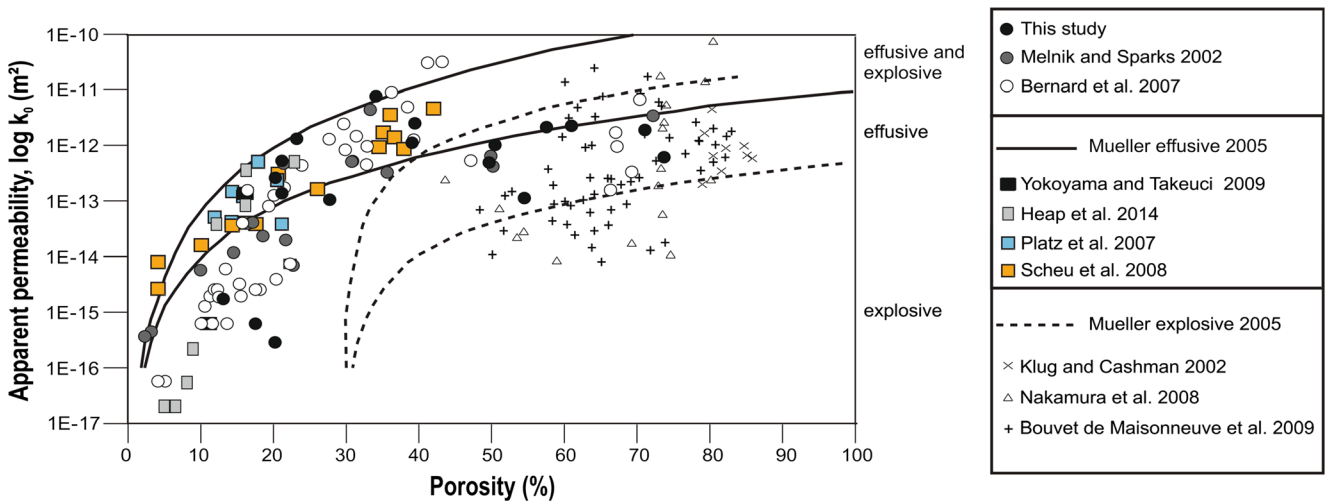


**Fig. 11** Bulk porosity vs. apparent permeability together with data from previous studies based on permeability measurements of silicic tephras (Melnik and Sparks 2002; Klug et al. 2002; Bernard et al. 2007; Platz

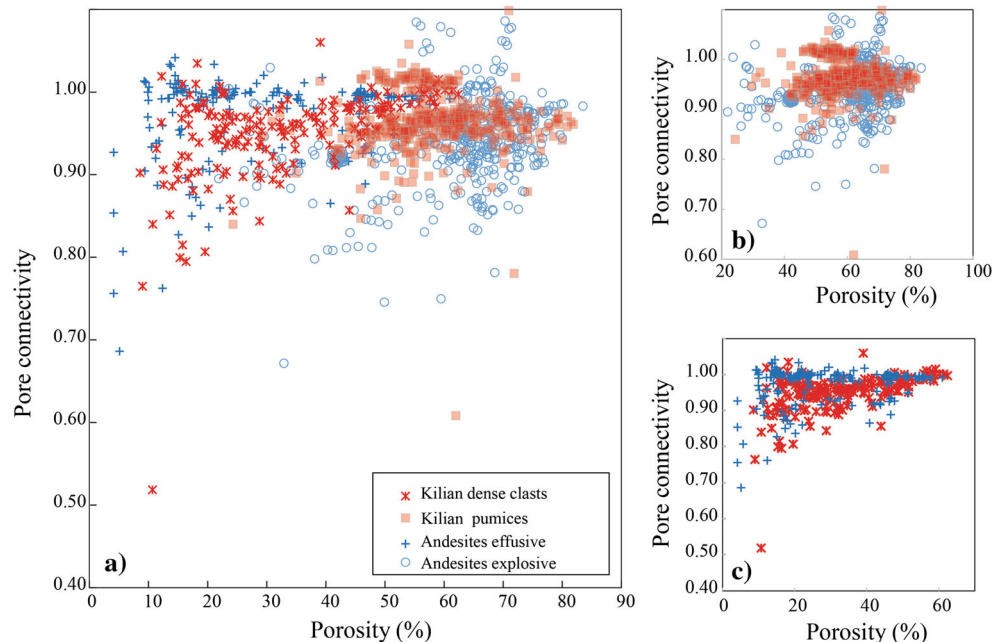
et al. 2007; Nakamura et al. 2008; Yokoyama and Takeuchi 2009, Bouvet de Maisonneuve et al. 2009; Heap et al. 2014)

eruption (Adams et al. 2006), both in the wide range and bimodality of their distributions. In contrast, the unimodal distributions of units U2 and U3 more resemble those from the subplinian eruptions of Augustine 1986, Kelut 1990 (Mueller et al. 2011), and Chaiten 2008 (Alfano et al. 2012), although in those cases, the modes lie at lower densities than those of U2 and U3. A shift of the vesicular mode toward higher densities has been attributed to a decrease of eruption intensity (Mueller et al. 2011) and/or because the presence of high abundance of crystals in Kilian products in respect to the aphyric pumice of Chaiten, for example. We conclude that the Kilian pyroclasts most resemble those from vulcanian to low-intensity subplinian explosions at other volcanoes. Explosions

U1, K1, and K2 took place from conduits plugged by (and partially lined by) degassed magma and/or lava, whereas U2 and U3 took place from conduits with plugs too thin to generate a discrete population of dense pyroclasts. The presence of abundant pumice in the Kilian deposit distinguishes it from the deposits from lateral explosions of domes/cryptodomes, which lack of pumice (Fig. 10).

This interpretation is reinforced by comparison of the Kilian pyroclasts with those from other silicic eruptions on the plot of permeability versus porosity (Fig. 11). Despite the simplifications of, and problems inherent in permeability models based on percolation theory, the explosive and effusive trends of Mueller et al. (2005) are also shown as

**Fig. 12** **a** Pore connectivity (expressed as a fraction) versus bulk porosity of Kilian pyroclasts compared with effusive (blue crosses) and explosive (blue open circles) andesites from the literature (Formenti and Druitt 2003; Mueller et al. 2005; Platz et al. 2007; Bernard et al. 2007; Giachetti et al. 2010; Farquharson et al. 2015). **b** Explosive andesite samples plus Kilian pumice. **c** Effusive andesite samples plus Kilian dense clasts



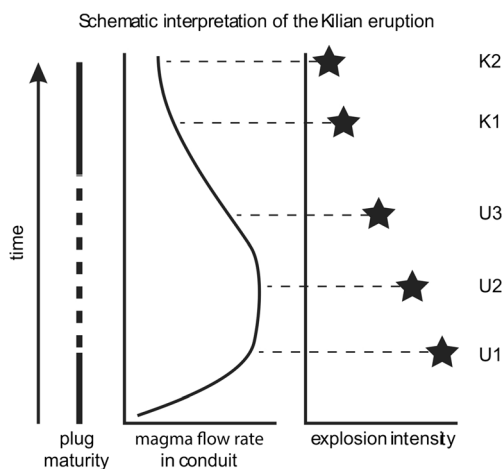


**Fig. 13** Schematic interpretation of the Kilian eruption

general guides in this figure. However, it must be noted that a unique percolation threshold at  $\Phi$  approaching 30% for the explosive rocks is very simplistic (e.g., Rust and Cashman 2011). Consequently, a significant number of effusive rocks are displaced toward higher porosity values at a given permeability value, compared to the effusive field (e.g., Wright et al. 2009). The Kilian pumices fall in the field of pumices from plinian (Klug et al. 2002; Nakamura et al. 2008; Bouvet de Maisonneuve et al. 2009) or vulcanian (Melnik and Sparks 2002; Bernard et al. 2007) eruptions, and they overlap the explosive trend predicted by the percolation theory (Mueller et al. 2005). On the other hand, the dense Kilian pyroclasts resemble those of dense samples of lava domes from Montserrat, Montagne Pelée, Unzen, Mount Taranaki/Egmont, Colima, and Asama, sampled either in situ or in block and ash flow deposits (Melnik and Sparks 2002; Bernard et al. 2007; Platz et al. 2007; Scheu et al. 2008; Yokoyama and Takeuchi 2009; Heap et al. 2014), and they follow the effusive trend of Mueller et al. (2005). Very similar information can be observed in Fig. 12a, where we show the pore connectivity relationship with porosity for Kilian pyroclasts, separated macroscopically into dense clasts and pumices. In addition, we compare our data to those from the literature on andesitic pumices (Fig. 12a, b) and dense rocks (Fig. 12a, c) from domes, lavas, and block and ash flows (Formenti and Druitt 2003; Mueller et al. 2005; Platz et al. 2007; Bernard et al. 2007; Giachetti et al. 2010; Farquharson et al. 2015). We observe that the dense trachytes nicely encompass the field of the dense andesites, confirming that they also derived from a shallow degassed dome. On the other hand, the trachytic pumices form a cluster with similar ranges of connectivity and porosity as for andesitic pumices.

The distinct permeability and connectivity trends for effusive rocks compared to the explosive rocks might be explained by two processes both leading to outgassing: (i) a hysteresis cycle with an initial vesiculation stage and the

formation of a connected and permeable porous network, followed by gas escape, bubble collapse, and further densification leading to a reduction of permeability with porosity (Rust and Cashman 2004) or (ii) an increase of permeability with porosity at a very low percolation threshold by a combination of bubble coalescence and fracturing in a highly crystalline magma (Bernard et al. 2007, Wright et al. 2006). The onset of connectivity and permeability can occur at a much lower percolation threshold in the case of high crystallinities that favor bubble coalescence (e.g., Blower 2001; Oppenheimer et al. 2015) or in the presence of abundant cracks (Mueller et al. 2005), both criteria being encountered in the dense pyroclasts (Fig. 6e–i). From the observed textures, we propose that the dominant process leading to outgassing seems to be a combination of bubble coalescence enhanced by the high crystallinity of the dense clasts, combined with extensive fracturing. However, a hysteresis with bubble collapse cannot be completely discarded here despite the absence of textural evidence.

### Bubble nucleation and growth

The size distribution spectra of vesicles provide time-integrated records of nucleation, growth, and coalescence ( $\pm$  collapse) of bubbles during magma ascent, fragmentation, and eruption. Kilian pyroclasts of all porosities contain a population of small vesicles (mode 1–600  $\mu\text{m}$ ); the most vesicular samples also contain a second distinct population of much larger vesicles (mode 600–5000  $\mu\text{m}$ ), which is absent in the dense clasts (Fig. 7). In one dense clast (U1\_b\_96), the small vesicle population extends to smaller dimensions (mode < 1–20  $\mu\text{m}$ ). A key observation in interpreting the origin of these two populations is that the small population is present both in magmas derived from the shallow, outgassed levels of the conduit (dense pyroclasts) as well as in magma derived from deeper levels (pumice). This suggests that the small vesicle population has a common origin in pyroclasts of all porosities and is related to the sudden decompression accompanying explosion onset.

The population of large vesicles in the pumices, on the other hand, may (1) come from a rapid episode of vesicle coalescence from the small, syneruptive population or (2) may be pre-eruptive vesicles formed by bubble growth and coalescence during slow viscous ascent prior to explosion onset. We favor the second explanation, since it is unclear how syneruptive coalescence could generate such discrete mode of very large vesicles.

The number densities ( $N_v$ ) of each vesicle population are consistent with these interpretations. Experiments on silicic melts have shown that  $N_v$  immediately following bubble nucleation is a function of magma decompression rate (e.g., Mourtada-Bonnefoi and Laporte 2004; Toramaru 2006; Cluzel et al. 2008). Hence, the higher the  $N_v$ , the higher the

decompression rate experienced by the melt during bubble nucleation, although coalescence will subsequently cause  $N_v$  to drop.  $N_v$  for the small population is  $\sim 10^6 \text{ mm}^{-3}$  in all pyroclasts except in dense clast U1\_b\_96, in which it is two orders of magnitude higher (Table 6). This implies that the decompression rate driving the nucleation of small vesicles was very high, consistent with a syn-eruptive origin. On the other hand,  $N_v$  of large vesicles is much lower ( $10^{-2} \text{ mm}^{-3}$ , Table 6), consistent with nucleation during slow viscous ascent and coalescence prior to explosion onset. An important observation is that the small vesicles in Kilian pyroclasts are almost always attached to Fe-Ti oxide microlites, emphasizing the importance of heterogeneous bubble nucleation in the trachytic melt. Fe-Ti oxides are the main mineral phase that acts as an energetically favorable nucleation site for gas bubbles (Hurwitz and Navon 1994). This is particularly striking in the dense clasts, in which most nanometric to micrometric vesicles are associated with Fe-Ti oxides on SEM images. The number density of Fe-Ti oxides,  $N_{\text{oxides}}$ , measured with FOAMS is lower, or of the same order of magnitude as  $N_v$  (Table 4), but is probably underestimated as explained earlier.  $N_{\text{oxides}}$  in clast U1\_b\_96 is significantly higher than for other Kilian clasts with nanometric oxides revealed by the SEM images, explaining the high  $N_v$  of very small bubbles in this sample. The good correspondence between the oxide and vesicle size modes in dense clasts (in which bubble expansion is not important) also emphasizes the importance of heterogeneous nucleation (Fig. 7). Significant bubble growth has decoupled the modes of oxides and vesicles in pumice.

Microlite growth during melt outgassing also influenced bubble growth, sizes, shapes, and distributions (e.g., Belien et al. 2010). In our study, microlite size range seems to occur between 10 and 100  $\mu\text{m}$ , which corresponds nearly to the main small vesicle mode in pumices. This suggests that expansion of the small bubbles was spatially limited by the microlites.

### Comparison with other eruptions

Products of the Kilian Volcano (KV) bear many similarities to those of the 1997 Vulcanian explosions of Soufrière Hills Volcano (SHV), Montserrat in 1997, which have been described in a number of publications (Druitt et al. 2002; Formenti and Druitt 2003; Clarke et al. 2007; Giachetti et al. 2010, 2011; Burgisser et al. 2010). The similarities include (1) repeated, short-lived explosions accompanied by ballistic showers; (2) pyroclasts with a wide range of porosities, ranging from dense (plug/dome-derived) to pumiceous (conduit-derived); (3) populations of large, pre-eruptive vesicles and small, syneruptive vesicles; (4) heterogeneous nucleation of syneruptive bubbles on Fe-Ti oxide grains; and (5) eruption through an existing lava dome. Differences between the two eruptions are (1) the different magma compositions (trachytic

at KV, andesitic SHV), (2) the number of major explosions ( $\sim 5$  at KV,  $\sim 80$  at SHV), and (3) the scarcity of well-defined breadcrust bombs with glassy rims at KV. The presence of abundant pumice and close similarity of products to those at SHV lead us to rule out a dominant role of water-magma interaction in the Kilian explosions (Camus 1975; Camus et al. 1975; Michon 1996), except perhaps in any minor opening phase. Like at SHV in 1997, the main Kilian explosions were magmatically driven. The combination of product characterization with detailed eruption measurements now allows us to exploit the Montserrat analogy (Giachetti et al. 2010) in reconstructing events at KV. It must of course be kept in mind that the section of Coupe des Muletiers, although significantly more developed than any other known outcrop, probably may not record all the eruptive events.

### Reconstruction of events prior to and during the 9.4-ka eruption

The Kilian eruption took place from the NW margin of an uplifted and faulted area (Puy Grosmanaux, Fig. 1b) that has been attributed to an underlying cryptodome (van Wyk de Vries et al. 2014 and Fig. 1c). Prior to the eruption, 775 °C trachytic magma ascended slowly from a reservoir at 300–400 MPa (Martel et al. 2013). The first vulcanian-subplinian explosion (U1) began when the overpressure of the magma column beneath the degassed plug or dome reached a critical threshold that caused the explosion (Druitt et al. 2002; Melnik and Sparks 2002). This rapid decompression of the magma caused heterogeneous nucleation of a high number density of small bubbles on Fe-Ti oxide grains, followed by rapid decompression growth. The fragmentation front descended into the conduit, ejecting first the dense fragments of the plug, then more vesicular magma from progressively deeper in the conduit. The dense plug fragments were ejected immediately into the atmosphere, where they quenched rapidly, impeding a significant growth of the bubbles. Bubble growth in the plug fragments was also limited due to the high abundance of microlites. In contrast, the longer time between decompression and eruption quench enabled greater growth of syneruptive bubbles in the pumiceous magma deeper in the conduit. Conduit drawdown progressed until conditions were no longer suitable for fragmentation. Although this depth cannot be estimated, it is notable that the proportion of dense to pumiceous pyroclasts remains approximately constant up through unit U1 (Fig. 3c). Hence, the explosion reamed out the upper conduit in a way that outgassed magma (plug, conduit sidewalls) and gas-rich, deeper magma were ejected in approximately constant proportions. Fragments of non-juvenile lava and basement granite may have been eroded from the conduit walls and/or picked up off the ground from older ejecta by pyroclastic density currents. The explosion

generated a 2-m-thick reversely to normally graded layer at the Coupe des Muletiers location.

Following the first explosion, at least four more major explosions occurred, separated by pauses of unconstrained duration. Decreasing thickness and maximum grain size upwards at the Coupe des Muletiers (Fig. 1a, b) suggest that these four explosions were less intense than the first one and that overall the explosion intensity decreased with time.

The first two explosions generated currents with a significant lateral component, which resulted in emplacement of pyroclastic density current deposits (Fig. 2). The last three explosions generated significant fallout on the summit of the pre-existing Puy de Dôme lava dome immediately to the north. Explosions U1, K1, and K2 discharged abundant dense pyroclasts, as well as pumice, generating deposits with bimodal density distributions. This implies that these explosions were preceded by the formation of a plug that capped the vent and that the magma ascended slowly enough to allow shallow outgassing through permeable pathways. Explosions U2 and U3, on the other hand, generated pyroclasts with unimodal density distributions and little dense juvenile debris, suggesting that the decompression rate must have been too fast prior to these explosions to allow extensive shallow outgassing. A low abundance of ejected non-juvenile clasts also characterized explosions U2 and U3 (Fig. 3c), suggesting limited conduit wall rock erosion, perhaps due to lower pre-explosion pressure buildup.

Our interpretation is that the eruption evolved in three stages (Fig. 13): (1) the magma ascent was slowed by the plug, which generated a strong overpressure that caused a powerful explosion from beneath a well-developed plug (U1), (2) loss of the plug, in turn, allowed downward propagation of the decompression wave to generate the more vesicular (less crystalline) material of U2 and U3, and (3) a waning phase of slow magma ascent and two weak explosions (K1, K2) from beneath thick plugs.

## Conclusions

1. The 9.4-ka Kilian eruption took place on the edge of a cryptodome and involved five main explosions with accompanying ballistic showers.
2. The eruption evolved in three stages: (1) strong overpressure of the magma column beneath the degassed plug or dome that reached a critical threshold that caused the powerful explosion of a well-developed plug, (2) the loss of the plug allowed downward propagation of a decompression wave that produced two less-powerful explosions from beneath much thinner plugs, and (3) a waning phase of slow magma ascent and two weak explosions from beneath thick plugs.

3. The three plug-confined explosions discharged trachytic pyroclasts of a wide range of porosities, with bimodal density distributions similar to those from vulcanian explosions elsewhere; pyroclasts from the other two explosions have unimodal density distributions at intermediate values, more typically produced by subplinian events.
4. Pyroclasts of all densities contain a population of small vesicles with exponential cumulative size distributions and high number densities interpreted to have formed during rapid explosion-driven decompression. Incipient coalescence of these syneruptive bubbles formed a coarse, power-law tail on the distribution of this population. An additional population of large, low-number-density vesicles probably formed deep in the conduit during slow viscous ascent of the magma prior to each explosion.
5. Connectivity and permeability relationships with porosity confirm that dense clasts arose from outgassing and effusive activity and originated from a shallow plug. We propose that coalescence, enhanced by the high crystallinity in the plug, combined with pervasive fracturing, was most likely responsible for increasing the permeability and allowing subsequent outgassing in the dense plug, in agreement with the observed textures. On the other hand, an initial vesiculation followed by gas escape, bubble collapse, and resulting reduction of permeability is also compatible with our results.
6. The eruption and its products bear many similarities to the 1997 explosive eruptions and their products at Soufrière Hills Volcano, Montserrat.

**Acknowledgments** The digital terrain model of Fig. 1 was extracted from a wider Lidar survey provided by a collective project driven by the Centre Régional Auvergnat de l'Information Géographique (CRAIG), which was supported financially by the Conseil Général du Puy-de-Dôme, the Fond Européen de Développement Régional (FEDER), and Blaise Pascal University of Clermont-Ferrand. We thank editor K. Cashman as well as the two reviewers, T. Giachetti and H.M.N. Wright, for thoughtful and constructive comments on the manuscript. This research was financed by the French Government Laboratory of Excellence initiative no. ANR-10-LABX-0006, the Région Auvergne, and the European Regional Development Fund. This is Laboratory of Excellence Clervolc contribution number 232.

## References

- Adams NK, Houghton BF, Hildreth W (2006) Abrupt transitions during sustained explosive eruptions: examples from the 1912 eruption of Novarupta, Alaska. *Bull Volcanol* 69(2):189–206
- Alfano F, Bonadonna C, Gurioli L (2012) Insights on rhyolitic eruption dynamic from textural analysis: the example of the May Chaitén eruption (Chile). *Bull Volcanol* 74:2095–2108. doi:10.1007/s00445-012-0648-3
- Barberi F, Cioni R, Santacroce R, Sbrana A, Vecci R (1989) Magmatic and phreatomagmatic phases in explosive eruptions of Vesuvius as deduced by grain-size and component analysis of the pyroclastic deposits. *J Volcanol Geotherm Res* 38:287–307

- Barker SJ, Rotella MD, Wilson CJ, Wright IC, Wysoczanski RJ (2012) Contrasting pyroclast density spectra from subaerial and submarine silicic eruptions in the Kermadec arc: implications for eruption processes and dredge sampling. *Bull Volcanol* 74(6):1425–1443
- Baudry D, Camus G (1972) Les projections volcaniques de la Chaîne des Puys et leurs utilisations. *Géol appl, chrono des mines, Bull BRGM* 2 ème ser, sect 2, 2:104p
- Befus KS, Zinke RW, Jordan JS, Manga M, Gardner JE (2014) Pre-eruptive storage conditions and eruption dynamics of a small rhyolite dome: Douglas Knob, Yellowstone volcanic field, USA. *Bull Volcanol* 76:808. doi:10.1007/s00445-014-0808-8
- Belien IB, Cashman KV, Rempel AW (2010) Gas accumulation in particle-rich suspensions and implications for bubble populations in crystal-rich magma. *Earth Planet Sci Lett* 297:133–140
- Belousov A, Voight B, Belousova M (2007) Directed blasts and blast-generated pyroclastic density currents: a comparison of the Bezymianny 1956, Mount St Helens 1980, and Soufrière Hills, Montserrat 1997 eruptions and deposits. *Bull Volcanol* 69(7):701–740
- Bernard ML, Zamora M, Géraud Y, Boudon G (2007) Transport properties of pyroclastic rocks from Montagne Pelée volcano (Martinique, Lesser Antilles). *J Geophys Res* 112:B05205. doi:10.1029/2006JB004385
- Bernard B, Kueppers U, Ortiz H (2015) Revisiting the statistical analysis of pyroclast density and porosity data. *Solid Earth* 6:869–879. doi:10.5194/se-6-869-2015
- Blower JD (2001) A three-dimensional network model of permeability in vesicular material. *Comput Geosci* 27:115–119
- Boivin P, Thouret JC (2013) The volcanic Chaîne des Puys: a unique collection of simple and compound monogenetic edifices. In: Fort M, André MF (Eds.), *Landscapes and landforms of France*. 9. Springer, Heidelberg, pp. 81–91
- Boivin P, Besson JC, Briot D, Camus G, de Goër de Herve A, Gourgaud A, Labazuy P, Langlois EP, de Larouzière FD, Livet M, Mergoil J, Miallier D, Morel JM, Vernet G, Vincent PM (2009) *Volcanologie de la Chaîne des Puys* (ed. Parc Naturel Régional de la Chaîne des Puys). Map 1/125,000 and booklet, 196 p
- Boivin P, Miallier D, Cluzel N, Devidal J-L, Dousteyssier B (2015) Building and ornamental use of trachyte in the center of France during antiquity: sources and criteria of identification. *J Archaeol Science: Rep* 3:247–256. doi:10.1016/j.jasrep.2015.06.017
- Boudon G, Balcone-Boissard H, Villemant B, Morgan DJ (2015) What factors control superficial lava dome explosivity? *Sci Rep* 5:14551. doi:10.1038/srep14551
- Bouvet de Maisonneuve C, Bachmann O, Burgisser A (2009) Characterization of juvenile pyroclasts from the Kos Plateau Tuff (Aegean Arc): insights into the eruptive dynamics of a large rhyolitic eruption. *Bull Volcanol* 71:643–658. doi:10.1007/s00445-008-0250-x
- Burgisser A, Poussineau S, Arbaret L, Druitt TH, Giachetti T, Bourdier JL (2010) Pre-explosive conduit conditions of the 1997 Vulcanian explosions at Soufrière Hills Volcano (Montserrat): I. Pressure and vesicularity distributions. *J Volcanol Geotherm Res* 194(1–3):27–41. doi:10.1016/j.jvolgeores.2010.01.008
- Burgisser A, Arbaret L, Druitt TH, Giachetti T (2011) Pre-explosive conduit conditions of the 1997 Vulcanian explosions at Soufrière Hills Volcano, Montserrat: II Overpressure and depth distributions. *J Volcanol Geotherm Res* 199:193–205. doi:10.1016/j.jvolgeores.2010.11.014
- Camus G (1975) *La Chaîne des Puys (Massif Central Français): Etude structurale et volcanologique*, PhD thesis, University of Clermont-Ferrand
- Camus G, Goër de Herve A, Kieffer G, Mergoil J, Vincent PM (1975) *Volcanologie de la Chaîne des Puys*. Parc Naturel Régional des Volcans d'Auvergne Clermont-Ferrand, 112 p, + 1/25 000 map
- Carey RJ, Houghton BF, Thordarson T (2009) Abrupt shifts between wet and dry phases of the 1875 eruption of Askja Volcano: microscopic evidence for macroscopic dynamics. *J Volcanol Geotherm Res* 184:256–270
- Cas RAF, Wright JV (1987) *Volcanic successions: modern and ancient*. Allen & Unwin, London 528 p
- Castro JM, Cordonnier B, Tuffen H, Tobin MJ, Puskar L, Martin MC, Bechtel HA (2012) The role of melt-fracture degassing in defusing explosive rhyolite eruptions at volcan Chaiten. *Earth Planet Sci Lett* 333-334:63–69. doi:10.1016/j.epsl.2012.04.024
- Clarke AB, Stephens S, Teasdale R, Sparks RSJ, Diller K (2007) Petrologic constraints on the decompression history of magma prior to Vulcanian explosions at the Soufrière Hills volcano, Montserrat. *J Volcanol Geotherm Res* 161(4):261–274
- Cluzel N, Laporte D, Provost A, Kannewischer I (2008) Kinetics of heterogeneous bubble nucleation in rhyolitic melts: implications for the number density of bubbles in volcanic conduits and for pumice textures. *Contrib Mineral Petrol* 156(6):745–763
- Colombier M (2013) *Analyse texturale des produits vulcaniens du Puy Kilian, Chaîne des Puys, France*. Mémoire de Master 2 recherche, Université Blaise Pascal. 49 p
- Couch S, Sparks RSJ, Carroll MR (2003) The kinetics of degassing induced crystallization at Soufrière Hills Volcano, Montserrat. *J Petrol* 44:1477–1502
- Degruyter W, Bachmann O, Burgisser A, Manga M (2012) The effects of outgassing on the transition between effusive and explosive silicic eruptions. *Earth Planet Sci Lett* 349-350:161–170
- Di Traglia F, Cimarelli C, De Rita D, Gimeno Torrente D (2009) Changing eruptive styles in basaltic explosive volcanism: examples from Croscat complex scoria cone, Garrotxa Volcanic Field (NE Iberian Peninsula). *J Volcanol and Geoth Res* 180:89–109. doi:10.1016/j.jvolgeores.2008.10.020
- Druitt TH, Young SR, Baptie B, Bonadonna C, Calder ES, Clarke AB, Voight B (2002) Episodes of cyclic Vulcanian explosive activity with fountain collapse at Soufrière Hills Volcano, Montserrat. *Geol Soc London Mem* 21(1):281–306
- Eychenne J, Houghton BF, Swanson DA, Carey RJ, Swavely L (2015) Dynamics of an open basaltic magma system: the 2008 activity of the Halema'uma'u Overlook vent, Kilauea Caldera. *Earth Planet Sci Lett* 409:49–60
- Fagents SA, Gregg TKP, Lopes RMC (2013) *Modeling volcanic processes. The physics and mathematics of volcanism*. Cambridge University Press, Cambridge. Cambridge Books Online
- Fanara S, Behrens H, Zhang Y (2013) Water diffusion in potassium-rich phonolitic and trachytic melts. *Chem Geol* 346:149–161. doi:10.1016/j.chemgeo.2012.09.030
- Farquharson J, Heap MJ, Varley NR, Baud P, Reuschlé T (2015) Permeability and porosity relationships of edifice-forming andesites: a combined field and laboratory study. *J Volcanol Geotherm Res* 297:52–68. doi:10.1016/j.jvolgeores.2015.03.016
- Fisher RV, Schmincke H-U (1984) *Pyroclastic rocks*. Springer, Berlin Heidelberg New York
- Formenti Y, Druitt TH (2003) Vesicle connectivity in pyroclasts and implications for the fluidisation of fountain-collapse pyroclastic flows, Montserrat (West Indies). *Earth Planet Sci Lett* 214(3):561–574
- Freundt A, Rosi M (1998) *From magma to tephra*. Elsevier, New York
- Giachetti T, Druitt TH, Burgisser A, Arbaret L, Galven C (2010) Bubble nucleation, growth and coalescence during the 1997 Vulcanian explosions of Soufrière Hills Volcano, Montserrat. *J Volcanol Geoth Res* 193(3):215–231
- Giachetti T, Burgisser A, Arbaret L, Druitt TH, Kelfoun K (2011) Quantitative textural analysis of Vulcanian pyroclasts (Montserrat) using multi-scale X-ray computed microtomography: comparison with results from 2D image analysis. *Bull Volcanol* 73(9):1295–1309. doi:10.1007/s00445-011-0472-1
- Glangeaud P (1913) *La Chaîne des Puys et la Petite Chaîne des Puys*. Librairie polytechnique, ch. Béranger Ed 135:241–496

- Goër de Herve A, Camus G, Boivin P, Gourgaud A, Kieffer G, Mergoïl J, Vincent, P-M (1994) Volcanology of the Chaîne des Puys [English traduction by C. Litto-de Goer of: "Volcanologie de la Chaîne des Puys, notice explicative de la carte 1:25000. 3th ed. up to dated"]. Parc Naturel Régional des Volcans d'Auvergne. Montlosier, Aydat. 127 p
- Gonnermann HM, Houghton BF (2012) Magma degassing and fragmentation during the plinian eruption of Novarupta, Alaska, 1912. *Geochem Geophys Geosyst* 13:Q10009. doi:10.1029/2012GC004273
- Gonnermann HM, Manga M (2007) The fluid mechanics inside a volcano. *Annu Rev Fluid Mech* 39:321–356
- Guérin G (1983) La thermoluminescence des plagioclases, méthode de datation du volcanisme. Applications au domaine volcanique français: Chaîne des Puys, Mont Dore et Cézallier, Bas Vivarais. Doctorat d'Etat, université Pierre et Marie Curie, Paris VI, 253 p
- Gurioli L, Harris AJL, Houghton BF, Polacci M, Ripepe M (2008) Textural and geophysical characterization of explosive basaltic activity at Villarrica volcano. *J Geophys Res* 113. doi:10.1029/2007JB005328
- Gurioli L, Andronico D, Bachelery P, Balcone-Boissard H, Battaglia J, Boudon G, Burgisser A, Burton MR, Cashman K, Cichy SB, Cioni R, Di Muro A, Dominguez L, D'Oriano C, Druitt T, Harris AJL, Hort M, Kelfoun K, Komorowski JC, Kueppers U, Le Pennec JL, Menand T, Paris R, Pioli L, Pistolesi M, Polacci M, Pompilio M, Ripepe M, Roche O, Rose-Koga E, Rust A, Scharff L, Schiavi F, Sulpizio R, Taddeucci J, Thordarson T (2015) MeMoVolc consensual document: a review of cross-disciplinary approaches to characterizing small explosive magmatic eruptions. *Bull Volcanol* 77:49. doi:10.1007/s00445-015-0935-x
- Hammer JE, Cashman KV, Hoblitt RP, Newman S (1999) Degassing and microlite crystallization during pre-climactic events of the 1991 eruption of Mt. Pinatubo, Philippines. *Bull Volcanol* 60(5):355–380
- Heap MJ, Lavallée Y, Petrakova L, Baud P, Reuschlé T, Varley NR, Dingwell DB (2014) Microstructural controls on the physical and mechanical properties of edifice-forming andesites at Volcán de Colima, Mexico. *J Geophys Res Solid Earth* 119:925–2963. doi:10.1002/2013JB010521
- Heiken G, Wohletz KH (1985) Volcanic ash. University of California Press, Berkeley
- Hoblitt RP, Harmon RS (1993) Bimodal density distribution of cryptodome dacite from the 1980 eruption of Mount St. Helens, Washington. *Bull Volcanol* 55(6):421–437
- Houghton BF, Wilson CJN (1989) A vesicularity index for pyroclastic deposits. *Bull Volcanol* 51(6):451–462
- Houghton BF, Wilson CJN, Del Carlo P, Coltelli M, Sable JE, Carey RJ (2004) The influence of conduit processes on changes in style of basaltic Plinian eruptions: Tarawera 1886 and Etna 122 BC. *J Volcanol Geotherm Res* 137:1–14
- Houghton BF, Carey RJ, Cashman KV, Wilson CJN, Hobden BJ, Hammer JE (2010) Divers patterns of ascent, degassing, and eruption of rhyolite magma during the 1.8 ka Taupo eruption, New Zealand: evidence from clast vesicularity. *J Volcanol Geotherm Res* 195:31–47
- Hurwitz S, Navon O (1994) Bubble nucleation in rhyolitic melts: experiments at high pressure, temperature, and water content. *Earth Planet Sci Lett* 122:267–280
- Jaupart C (1996) Physical models of volcanic eruptions. *Chem Geol* 128: 217–227. doi:10.1016/0009-2541(95)00175-1
- Jaupart C, Allegre CJ (1991) Gas content, eruption rate and instabilities of eruption regime in silicic volcanoes. *Earth Planet Sc Lett Letters* 102:413–429
- Kennedy B, Spieler O, Scheu B, Kueppers U, Taddeucci J, Dingwell DB (2005) Conduit implosion during vulcanian eruptions. *Geology* 33(7):581–584
- Klug C, Cashman KV (1996) Permeability development in vesiculating magmas: implications for fragmentation. *Bull Volcanol* 58(2–3):87–100
- Klug C, Cashman KV, Bacon CR (2002) Structure and physical characteristics of pumice from the climatic eruption of Mount Mazama (Crater Lake), Oregon. *Bull Volcanol* 64:486–501
- Kueppers U, Scheu B, Spieler O, Dingwell DB (2005) Field-based density measurements as tool to identify pre-eruption dome structure: set-up and first results from Unzen volcano, Japan. *J Volcanol Geotherm Res* 141:65–75
- Leduc L, Gurioli L, Harris AJL, Colò L, Rose-Koga E (2015) Dynamics of a gas-dominated strombolian explosion. *Bull Volcanol* 77:8. doi:10.1007/s00445-014-0888-5
- Mangan MT, Sisson TW (2000) Delayed, disequilibrium degassing in rhyolite magma: decompression experiments and implications for explosive volcanism. *Earth Planet Sci Lett* 183:441–455
- Martel C (2012) Eruption dynamics inferred from microlite crystallization experiments: application to plinian and dome-forming eruptions of Mt. Pelee (Martinique, Lesser Antilles). *J Petrol*. doi:10.1093/petrology/egr076
- Martel C, Champallier R, Prouteau G, Pichavant M, Arbaret L, Balcone-Boissard H, Boudon G, Boivin P, Bourdier J-L, Scaillet B (2013) Trachyte phase relations and implication for magma storage conditions in the Chaîne des Puys (French Massif Central). *J Petrol*. doi:10.1093/petrology/egt006
- Martini J, Duret J-J (1965) Etude du niveau de cendres volcaniques des sédiments post-glaciaires récents des environs de Genève. *Arch Sci* 18(3):563–575
- Massol H, Jaupart C (1999) The generation of gas overpressure in volcanic eruptions. *Earth Planet Sc Lett Letters* 166:57–70
- Matteo VD, Carroll MR, Behrens H, Vetere F, Brooker RA (2004) Water solubility in trachytic melts. *Chem Geol* 213:187–196. doi:10.1016/j.chemgeo.2004.08.042
- Maury R, Brousse R, Villemant B, Joron J-L, Jaffrezic H, Treuil M (1980) Cristallisation fractionnée d'un magma basaltique alcalin: la série de la Chaîne des Puys (Massif Central, France). I. Pétrologie. *Bull Minéralogie* 103:250–266
- Melnik O, Sparks RSJ (2002) Dynamics of magma ascent and lava extrusion at Soufrière Hills Volcano, Montserrat. In: Druitt, T.H., Kokelaar, B.P. (Eds.), The eruption of Soufrière Hills Volcano, Montserrat, from 1995 to 1999. *Geol Soc London Mem*, pp. 153–171
- Miallier D, Pilleyre T, Sanzelle S, Boivin P, Lanos P (2012) Revised chronology of the youngest volcanoes of the Chaîne des Puys (French Massif Central). *Quaternaire* 23(4):283–290
- Miallier D, Boivin P, Dousteysier B, Labazuy P (2013a) L'origine de la roche mise en œuvre pour la construction du temple de Mercure, au sommet du Puy de Dôme, et les implications archéologiques. *J Roman Archaeol* 26:2–20
- Miallier D, Pilleyre T, Boivin P, Sanzelle S (2013b) L'éruption phréatomagmatique du Montchié, Chaîne des Puys, Massif Central français (13.6 ± 1,0 ka). *Quaternaire* 24(2):99–107
- Michon L (1996) Le cratère Kilian et le Puy de Vasset: mécanismes éruptifs et distinction des produits proximaux et distaux. Comparaison avec le cratère-lac Pavin et le Puy Chopine. Mémoire de Maîtrise, Université Blaise Pascal. 19 p
- Morrissey MM, Mastin LG (2000) Vulcanian eruptions. In: Sigurdsson H (ed) *Encyclopedia of volcanoes*. Academic Press, San Diego, CA, pp 463–475
- Mourtada-Bonnefoi CC, Laporte D (2004) Kinetics of bubble nucleation in a rhyolitic melt: an experimental study of the effect of ascent rate. *Earth Planet Sc Lett* 218(3):521–537
- Mueller S, Melnik O, Spieler O, Scheu B, Dingwell DB (2005) Permeability and degassing of dome lavas undergoing rapid decompression: an experimental determination. *Bull Volcanol* 67:526–538. doi:10.1007/s00445-004-0392-4

- Mueller S, Scheu B, Kueppers U, Spieler O, Richard D, Dingwell DB (2011) The porosity of pyroclasts as an indicator of volcanic explosivity. *J Volcanol Geotherm Res* 203:168–174
- Mujin M, Nakamura M (2014) A nanolite record of eruption style transition. *Geology* 42(7):611–614
- Nakamura M, Otaki K, Takeuchi S (2008) Permeability and pore-connectivity variation of pumices from a single pyroclastic flow eruption: implications for partial fragmentation. *J Volcanol Geotherm Res* 176:302–314
- Neill OK, Hammer JE, Izbekov PE, Belousova MG, Belousov AB, Clarke AB, Voight B (2010) Influence of pre-eruptive degassing and crystallization on the juvenile products of laterally directed volcanic explosions. *J Volcanol Geotherm Res* 198(1):264–274
- Nguyen CTH, Gonnermann M, Chen Y, Huber C, Maiorano AA, Gouldstone A, Dufek J (2013) Film drainage and the lifetime of bubbles. *Geochem Geophys Geosyst* 14:3616–3631. doi:10.1002/ggge.20198
- Nguyen CT, Gonnermann HM, Houghton BF (2014) Explosive to effusive transition during the largest volcanic eruption of the 20th century (Novarupta 1912, Alaska). *Geology* 42(8):703–706. doi:10.1130/G35593.1
- Noguchi S, Toramaru A, Shimano T (2006) Crystallization of microlites and degassing during magma ascent: constraints on the fluid mechanical behavior of magma during the Tenjo Eruption on Kozu Island. *Japan Bull Volcanol* 68:432–449. doi:10.1007/s00445-005-0019-4
- Oppenheimer J, Rust AC, Cashman KV, Sandnes B (2015) Gas migration regimes and outgassing in particle-rich suspensions. *Front Phys* 3:1–13. doi:10.3389/fphy.2015.00060
- Platz T, Cronin SJ, Cashman KV, Stewart RB, Smith IEM (2007) Transition from effusive to explosive phases in andesite eruptions—a case-study from the AD1655 eruption of Mt Taranaki, New Zealand. *J Volcanol Geotherm Res* 161:15–34. doi:10.1016/j.jvolgeores.2006.11.005
- Polacci M, Pioli L, Rosi M (2003) The Plinian phase of the Campanian Ignimbrite eruption (Phlegrean Fields, Italy): evidence from density measurements and textural characterization of pumice. *Bull Volcanol* 65:418–432
- Polacci M, Bouvet de Maisonneuve C, Giordano D, Piochi M, Mancini L, Degruyter W, Bachmann O (2014) Permeability measurements of Campi Flegrei pyroclastic products: an example from the Campanian Ignimbrite and Monte Nuovo eruptions. *J Volcanol Geotherm Res* 272:16–22
- Portal A, Gailler L, Labazuy P, Lénat J (2016) Geophysical imaging of the inner structure of a lava dome and its environment through gravimetry and magnetism. *J Volcanol Geotherm Res* 320:88–99. doi:10.1016/j.jvolgeores.2016.04.012
- Raynal JP, Vernet G, Vivent D (1998) Des volcans et des hommes depuis le dernier interglaciaire en Basse Auvergne (Massif Central, France). In: *Il sistema uomo-ambiente tra passato e presente. Centro universitario europeo per i beni culturali, Ravello, Italia, Edipuglia (Ed.)*, Bari, pp. 197–220
- Reimer PJ, Baillie MGL, Bard E, Bayliss A, Beck JW, Blackwell PG, Ramsey CB, Buck CE, Burr GS, Edwards RL, Friedrich M, Grootes M, Guilderson TP, Hajdas I, Heaton TJ, Hogg AG, Hughen KA, Kaiser KF, Kromer B, McCormac FG, Manning SW, Reimer RW, Richards DA, Southon JR, Talamo S, Turney CSM, Van der Plicht J, Weyhenmeyer CE (2009) IntCal09 and Marine09 calibration curves. *Radiocarbon* 51:1111–1150
- Rotella MD, Wilson CJN, Barker SJ, Cashman KV, Houghton BF, Wright IC (2014) Bubble development in explosive silicic eruptions: insights from pyroclast porosity textures from Raoul volcano (Kermadec arc). *Bull Volcanol* 76:826
- Rust AC, Cashman KV (2004) Permeability of vesicular silicic magma: inertial and hysteresis effects. *Earth Planet Sci Lett* 228(1–2):93–107
- Rust AC, Cashman KV (2011) Permeability controls on expansion and size distributions of pyroclasts. *J Geophys Res* 116:B11202
- Ruth D, Ma H (1992) On the derivation of the Forchheimer equation by means of the averaging theorem. *Transp Porous Media* 7:255–264
- Saubin E, Tuffen H, Gurioli L, Owen J, Castro JM, Berlo K, McGowan EM, Schipper CI, Wehbe K (2016) Conduit dynamics in transitional rhyolitic activity recorded by tuffsite vein textures from the 2008–2009 Chaitén eruption. *Frontiers in Earth Science*. doi:10.3389/feart.2016.00059
- Scheu B, Kueppers U, Mueller S, Spieler O, Dingwell DB (2008) Experimental volcanology on eruptive products of Unzen volcano. *J Volcanol Geotherm Res* 175:110–119
- Schipper CI, Castro JM, Tuffen H, James MR, How P (2013) Shallow vent architecture during hybrid explosive–effusive activity at Cordón Caulle (Chile, 2011–12): evidence from direct observations and pyroclast textures. *J Volcanol Geotherm Res* 262:25–37
- Shea T, Houghton BF, Gurioli L, Cashman KV, Hammer JE, Hobden B (2010a) Textural studies of vesicles in volcanic rocks: an integrated methodology. *J Volcanol Geotherm Res* 190:271–289
- Shea T, Houghton BF, Gurioli L, Cashman KV, Hammer JE, Hobden BJ (2010b) Textural studies of vesicles in volcanic rocks: an integrated methodology. *J Volcanol Geotherm Res* 190(3–4):271–289
- Shea T, Gurioli L, Houghton BF, Cioni R, Cashman KV (2011) Column collapse and generation of pyroclastic density currents during the AD 79 eruption of Vesuvius: the role of pyroclast density. *Geology* 39(7):695–698
- Shea T, Gurioli L, Houghton BF (2012) Transitions between fall phases and pyroclastic density currents during the AD 79 eruption at Vesuvius: building a transient conduit model from the textural and volatile record. *Bull Volcanol* 74(10):2363–2381
- Sheridan MF (1971) Particle-size characteristics of pyroclastic tuffs. *J Geophys Res* 76(23):5627–5634
- Sheridan MF, Marshall JR (1983) Interpretation of pyroclast surface features using SEM images. *J Volcanol Geotherm Res* 16:153–159
- Shimano T, Nakada S (2006) Vesiculation path of ascending magma in the 1983 and the 2000 eruptions of Miyakejima volcano, Japan. *Bull Volcanol* 68:549–566. doi:10.1007/s00445-005-0029-2
- Silva C (2008) Reconstruction and eruptive dynamics of the Holocene basaltic-andesitic Pucón Ignimbrite. PhD thesis, University of Clermont-Ferrand
- Slezin YB (2003) The mechanism of volcanic eruptions (a steady state approach). *J Volcanol Geotherm Res* 122(1–2):7–50
- Sparks SRJ (1976) Grain size variations in ignimbrites and implications for the transport of pyroclastic flows. *Sedimentology* 23:147–188
- Sparks RSJ (1978) Dynamics of bubble formation and growth in magmas—review and analysis. *J Volcanol Geotherm Res* 3(1–2):1–37
- Taddeucci J, Pompilio M, Scarlato P (2002) Monitoring the explosive activity of the July–August 2001 eruption of Mt. Etna (Italy) by ash characterization. *Geophys Res Lett* 29(8):1029–1032. doi:10.1029/2001GL014372
- Takeuchi S, Nakashima S, Akihiko Tomiya A (2008) Permeability measurements of natural and experimental volcanic materials with a simple permeameter: toward an understanding of magmatic degassing processes. *J Volcanol Geotherm Res* 177:329–339
- Toramaru A (2006) BND (bubble number density) decompression rate meter for explosive volcanic eruptions. *J Volcanol Geotherm Res* 154(3–4):303–316
- van Wyk de Vries B, Márquez A, Herrera R, Granja Bruña JL, Llanes P, Delcamp A (2014) Craters of elevation revisited: forced-folds, bulging and uplift of volcanoes. *Bull Volcanol* 76:875–895. doi:10.1007/s00445-014-0875-x
- Vernet G (2013) La séquence sédimentaire des Gravanches/Grizat: enregistrement d'évènements “catastrophiques” en Limagne d’Auvergne (Massif Central, France). *Quaternaire* 24(2):109–127

- Vernet G, Raynal JP (2008) La formation de Marsat et le téphra CF7, marqueurs distaux d'éruptions trachytiques violentes de la Chaîne des Puys au Boréal. *Quaternaire* 19(2):97–106
- Villemant B, Joron J-L, Jaffrezic H, Treuil M (1981) Distribution coefficients of major and trace elements: fractional crystallization in the alkali basalt series of Chaîne des Puys (Massif Central, France). *Geochim Cosmochim Acta* 45:1997–2016
- Walker GPL (1971) Grain-size characteristics of pyroclastic deposits. *J Geol* 79:696–714
- Walker GPL (1973) Explosive volcanic eruptions—a new classification scheme. *Geol Rundsch* 62:431–446
- White JDL, Houghton BF (2006) Primary volcanoclastic rocks. *Geology* 34:677–680. doi:[10.1130/G22346.1](https://doi.org/10.1130/G22346.1)
- Wilson L, Sparks RSJ, Walker GPL (1980) Explosive volcanic eruptions—IV. The control of magma properties and conduit geometry on eruption column behavior. *Geophys J Roy Astr Soc* 63:117–148
- Wohletz K (1983) Mechanisms of hydrovolcanic pyroclast formation: grain-size, scanning electron microscopy, and experimental studies. *J Volcanol Geotherm Res* 17:31–63
- Wohletz KH, Sheridan MF, Brown WK (1989) Particle size distributions and the sequential fragmentation/transport theory applied to volcanic ash. *J Geophys Res* 94:15703–15721
- Wright HMN, Roberts JJ, Cashman KV (2006) Permeability of anisotropic tube pumice: model calculations and measurements. *Geophys Res Lett* 33:L17316. doi:[10.1016/j.epsl.2009.01.02](https://doi.org/10.1016/j.epsl.2009.01.02)
- Wright HMN, Cashman KV, Rosi M, Cioni R (2007) Breadcrust bombs as indicators of vulcanian eruption dynamics at Guagua Pichincha volcano, Ecuador. *Bull Volcanol* 69(3):281–300
- Wright HMN, Cashman KV, Gottesfeld EH, Roberts JJ (2009) Pore structure of volcanic clasts: measurements of permeability and electrical conductivity. *Earth Planet Sci Lett* 280:93–104. doi:[10.1016/j.epsl.2009.01.023](https://doi.org/10.1016/j.epsl.2009.01.023)
- Yokoyama T, Takeuchi S (2009) Porosimetry of vesicular volcanic products by a water-expulsion method and the relationship of pore characteristics to permeability. *J Geophys Res* 114:B02201. doi:[10.1029/2008JB005758](https://doi.org/10.1029/2008JB005758)